



1 **Impact of meteorological and oceanographic conditions on the** 2 **state of sea ice in Hornsund, Svalbard over 23 years**

3
4 Vincent Papin¹, Zuzanna M. Swirad², A. Malin Johansson³, and Eirik Malnes⁴

5
6 ¹Faculty of Sciences and Technologies, University of Toulon, Toulon, France

7 ²Institute of Geophysics, Polish Academy of Sciences, Warsaw, Poland

8 ³Department of Physics and Technology, UiT The Arctic University of Norway, Tromsø, Norway

9 ⁴NORCE Research AS, Oslo, Norway

10 *Correspondence: Zuzanna M. Swirad (zswirad@igf.edu.pl) and A. Malin Johansson (malin.johansson@uit.no)*

11 **Abstract.** The full archive of historical SAR imagery at ~50 m resolution (Envisat ASAR, RADARSAT-2 and
12 Sentinel-1) capturing the Hornsund fjord, Svalbard was used to create an unprecedented set of near-daily binary
13 ice/open water maps over the fjord area for 23 seasons (2002-2025). We observe a general trend with the sea ice
14 season shortening by 2.3 days yr⁻¹, and a gradual decrease in average ice coverage, particularly in the main basin
15 of Hornsund (-1.6% yr⁻¹). The interannual ice condition variability was strongly related to the autumn (October-
16 December) and/or winter (January-March) air temperatures. The length of the sea ice season was shortened by
17 19.5 days for every 1°C increase in mean autumn air temperature ($R^2 = 0.61$, $p < 0.05$). Air temperature remained
18 under the freezing point for over 90 days before landfast ice freeze-up. Drift ice was present in the fjord before
19 the freeze-up with an average coverage exceeding 20% 40 days and 26% one day before the landfast ice onset.
20 The landfast ice season break-up period was characterised by a lack of drift ice, and positive air temperatures for
21 over a month. The day of landfast ice freeze-up and break-up overlapped with an average sea ice thickness of 0.33
22 m and 0.57 m as derived from thermodynamic terms, respectively, suggesting the importance of other processes.

23 **1 Introduction**

24
25 Awareness of climate change has developed gradually over the decades, as scientific advances have enabled a
26 better understanding of the impact of human activities on the climate. IPCC (2023) showed that the global surface
27 temperature was 1.09°C warmer during the period 2011-2020 compared to 1850-1900, primarily due to the
28 greenhouse gases, dominated by carbon dioxide and methane, partially offset by the cooling effect of aerosols.
29 The Arctic is one of the most affected regions, with a surface temperature increase of more than twice that of the
30 global average, and with some regions experiencing even higher increases (Jansen et al., 2020). Since the
31 beginning of satellite observations in 1978, sea ice coverage in the Arctic has significantly declined, reaching
32 exceptionally low levels in September 2012 (<https://nsidc.org/sea-ice-today/sea-ice-tools/charctic-interactive-sea-ice-graph>;
33 <https://nsidc.org/sea-ice-today/sea-ice-tools/charctic-interactive-sea-ice-graph>; last access: 16 March 2026). Svalbard is one of the fastest warming regions in the world, with warming
34 in both summer and winter being significant (van der Broek, 2025).

35
36 The reduction in sea ice cover contributes to the strengthening of surface winds, particularly in autumn and winter,
37 most likely due to the lower surface roughness of open water compared to sea ice (Mioduszewski et al., 2018).



38 This intensification of winds leads to increasing potential fetch and wave height in the region (Casas-Prat and
39 Wang, 2020). These changes result in increased coastal exposure to wave-induced erosion (Zagórski et al., 2015;
40 Herman et al., 2025). For Isfjorden, western Svalbard, the wind direction was found to affect the circulation pattern
41 and hence the ocean surface water temperature (Fraser et al., 2018).

42

43 In addition to its environmental impact, sea ice plays a crucial role in Arctic navigation. The extent and thickness
44 of sea ice directly affect the accessibility and safety of maritime routes in the polar region. With the decline of sea
45 ice, previously inaccessible routes, such as the Northern Sea Route and the Northwest Passage, are becoming
46 increasingly navigable during summer months (Smith and Stephenson, 2013). This change has led to increased
47 shipping activity in the Arctic (Pizzolato et al., 2016) and opens new opportunities for commercial shipping and
48 resource exploration. Stocker et al. (2020) investigated the connection between maritime operations and the sea
49 ice variability around Svalbard in 2012-2019, and found a clear correlation between the lack of sea ice and
50 increased maritime operations. Though the behaviour differed between the fishing vessels and the cruise ships in
51 change of location, where cruise ships sought to circumnavigate Spitsbergen and fishing vessels moved
52 northwards.

53

54 In coastal Arctic environments, sea ice conditions often differ from those observed in the open ocean due to strong
55 local controls. In sheltered bays landfast ice forms, but the factors influencing the formation and spatial extent of
56 the landfast ice differ regionally and are not fully understood (Itkin et al., 2015). The steep surrounding
57 topography, typical of Arctic fjords, can produce strong local contrasts in wind and near-surface air temperatures,
58 leading to distinct microclimates that influence ice formation processes (Frank et al., 2023). Fjord hydrography is
59 also complex, as oceanic inflows interact with freshwater input from glacier melt and rivers, leading to
60 stratification and circulation patterns that influence ice growth and break-up (Svendsen et al., 2002; Cottier et al.,
61 2010). Beyond their environmental importance, coastal sea ice plays a crucial role for local transportation such as
62 seasonal ice roads for community access, resource exploration and supply delivery (Dong et al., 2025). It also
63 provides temporary protection against wave-driven coastal erosion (Swirad et al., 2026a).

64

65 This study focuses on the analysis of fjord ice conditions in Hornsund, Svalbard. The main objectives are
66 threefold: (1) to produce binary ice/open water maps for Hornsund from the early 2000s up to the present day,
67 thereby establishing a consistent long-term record of sea ice conditions; (2) to characterize sea ice and landfast
68 ice seasons in terms of timing, duration and ice coverage; and (3) to identify the atmospheric and oceanic
69 conditions that govern landfast ice freeze-up and break-up in the fjord. Through this approach, the study aims to
70 improve our understanding of local-scale sea ice processes in Hornsund and contribute to a broader comprehension
71 of how Arctic coastal systems respond to ongoing climatic changes.

72 **2 Study area**

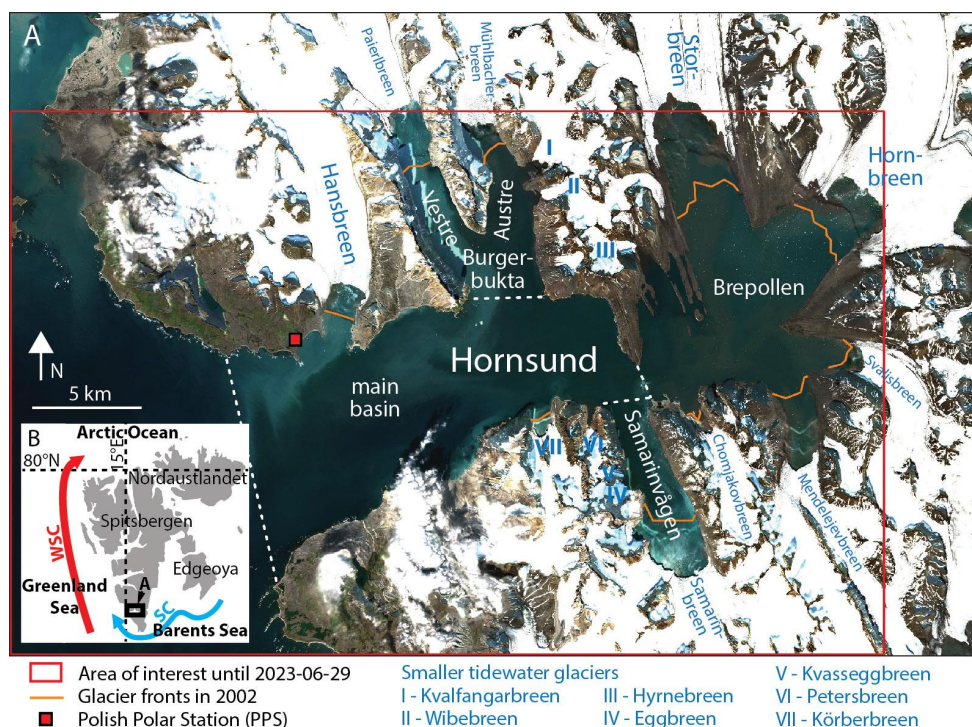
73 Hornsund is one of the smallest fjords of Spitsbergen, the largest island of the Svalbard archipelago, located in its
74 south-western part. It opens to the Greenland Sea in the west. The total area of Hornsund is about 320 km² with a
75 width of 12 km and a length of 34 km. Its average depth is approximately 100 m, although the maximum depth
76 can reach between 200-250 m in the main basin (Promińska et al., 2018).



77

78 The fjord consists of a main basin and several secondary bays, characterized by marine-terminating glaciers (Fig.
 79 1). These bays are Burgerbukta (Vestre and Austre) in the north, Brepollen in the east and Samarinvågen in the
 80 south. Brepollen is about 12 km long, connected to the outer fjord by a 2 km wide entrance. Samarinvågen is 7
 81 km long with an entrance 2 km wide, while Burgerbukta is 8 km long and an entrance of 4 km. A sill at 40-50 m
 82 divides Brepollen and Samarinvågen from the main basin significantly limiting water exchange between the two
 83 basins. Similarly there are sills at 25 and 30 m at the entrance to Austre and Vestre Burgerbukta, respectively
 84 (Jakacki et al., 2017).

85



86

87 **Figure 1. The study area: (a) Hornsund; (b) Svalbard. WSC – West Spitsbergen Current, SC – Sørkapp Current.**

88 **Background image: Sentinel-2 T33XWF_20250828T120701_TCI_10m scene.**

89

90 There are 16 tidewater glaciers in Hornsund (Błaszczuk et al., 2023; Fig. 1). Between 2001 and 2010, the glaciers
 91 retreated at a rate of 70 m yr⁻¹ which is significantly higher than the 45 m yr⁻¹ average for Svalbard (Błaszczuk et
 92 al., 2013). This glacier retreat has led to an increase in the fjord's surface area, from 188 km² in 1936 to 303 km²
 93 in 2010, as well as in its length, from 24 km in 1936 to 34 km in 2010 (Błaszczuk et al., 2013). Between 2012 and
 94 2017 Hansbreen, Storbreen and Hornbreen lost 11.8, 9.9 and 8.8% total area (Barzycka et al., 2020). Swirad et al.
 95 (2026b) calculated a total Hornsund area gain of 30 km² between 2011 and 2023 resulting from glacier retreat.
 96 The significant increase in glacier retreat in Hornsund has led to a rise in freshwater input to the fjord. During the
 97 period 2006-2015, Błaszczuk et al. (2019) estimated an average freshwater input to the Hornsund bays of 2517 ±
 98 82 Mt per year with the main contributions coming from glacier meltwater runoff (39%) and frontal ablation of



99 tidewater glaciers (25%). Secondly, total precipitation over land (excluding winter snowfall), total precipitation
100 over the fjord area and melting of the snow cover on unglaciated areas accounted for 21, 7 and 8%, respectively
101 (Błaszczuk et al., 2019).

102

103 Along the west coast of Spitsbergen, outside the fjords, the hydrological conditions and climate are mainly
104 influenced by the West Spitsbergen Current (WSC) carrying warm (3.5-6.0°C) saline (>35 g L⁻¹) Atlantic Water
105 (AW) and the Sørkapp Current (SC) carrying cold (-1.5 to 1.5°C) and fresher (34.3-34.8 g L⁻¹) Arctic Water (ArW)
106 (Swerpel, 1985; Jakacki et al., 2017; Fig. 1b). The SC carries drift ice from the eastern part of the Svalbard
107 Archipelago (Storfjorden) and the Barents Sea (Jakacki et al., 2017; Korhonen et al., 2024; Shulman et al., 2024).
108 In Hornsund, the presence of AW is relatively limited, however, Strzelewicz et al. (2021) reported an average
109 annual increase of 8% in the volume fraction of AW on the shelf between 1999 and 2020 with this trend becoming
110 especially pronounced during the last decade, a process referred to as Atlantification.

111

112 In Hornsund, the water circulation is cyclonic (anticlockwise) with inflow from the southwest and outflow to the
113 northwest. This circulation is mainly governed by tides and shelf currents (Jakacki et al., 2017). The tides are
114 semidiurnal with an amplitude ranging between 0.8 and 1.8 m (Kowalik et al., 2015; Promińska et al., 2018). A
115 statistically significant increase in storm frequency and the number of stormy days per year was observed at the
116 decadal scale outside the fjord (Wojtysiak et al., 2018). The complex configuration of the Hornsund coastline and
117 bathymetry causes strong wave modification through refraction and attenuation (Herman et al., 2019). The
118 significant wave height, H_s , varies by location – it reaches 1.2-1.3 m at the fjord's entrance, decreases to 0.5-0.9
119 m in the central part, and falls below 0.4 m in the inner areas (Swirad et al., 2023b). Since 2006, the seasonal
120 reduction in sea ice cover outside Hornsund has allowed more energetic waves to propagate into the fjord,
121 increasing their impact on coastal zones (Herman et al., 2025).

122

123 Herman et al. (2025) suggested that the decline in sea ice cover at the fjord entrance led to changes in the spatial
124 and seasonal distribution of wave energy. Zagórski et al. (2015) demonstrated shoreline retreat of 0.26 m yr⁻¹ in
125 Isbjørnhamna, where the Polish Polar Station (PPS) is located (Fig. 1b), between 1960 and 2011. This area has
126 shifted from a coastline formerly influenced by the nearby tidewater Hansbreen and the protection from persistent
127 sea ice and glacier ice to one increasingly exposed to storms and that is undergoing rapid transformation (Zagórski
128 et al., 2015). Additionally, the progressive degradation of permafrost and ground ice due to rising air temperatures
129 reduces the mechanical strength of coastal sediments, making them more vulnerable to erosion (Dobiński and
130 Kasprzak, 2022). Swirad et al. (2026a) observed near-zero net volume beach change in Isbjørnhamna between
131 2018 and 2025, but they observed existence of an erosional hotspot at the vicinity of the PPS infrastructure, and
132 a net accumulation at the eastern part of the bay.

133

134 Between 1979 and 2018, the mean annual air temperature at the PPS meteorological station was -3.7°C, with
135 March being the coldest (-10.2°C) and July – the warmest (4.6°C). Monthly mean temperatures in summer months
136 were relatively stable, typically around 5°C, whereas winter months showed much greater fluctuations with means
137 dropping below -10°C (Wawrzyniak and Osuch, 2020). This strong seasonal variability in winter is attributed to
138 alternating cold, stable anticyclonic subsidence and warmer, cyclonic disturbances (Rinke et al., 2017). The trend



139 in mean annual air temperature over the study period was $+1.14^{\circ}\text{C decade}^{-1}$, which is more than five times higher
 140 than the global average warming rate of $+0.17^{\circ}\text{C decade}^{-1}$ (NOAA, 2025; Wawrzyniak and Osuch, 2020). Dahlke
 141 et al (2020) investigated the air temperature change from 1980-2016 for the whole of Svalbard, finding a
 142 significant warming over Hornsund for 2010-2016 in January-March compared to the climatological records, with
 143 a $1^{\circ}\text{C decade}^{-1}$ annual warming and a December-February warming of $2.8^{\circ}\text{C decade}^{-1}$. Moreover, they found a
 144 statistically significant sea ice coverage reduction for the months of February-May for 1998-2016, a statistically
 145 significant reduction in May for 1980-1998, though no statistically significant change for 1980-2016. They also
 146 observed a reduced impact of wind and ice drift on the total sea ice extent around Svalbard, and that the surface
 147 air temperature has a larger impact on the extent.

148

149 Winds in Hornsund are influenced by the fjord's specific longitudinal shape, its proximity to the coastline and
 150 local topography. The prevailing winds are from the east with a mean annual wind speed of 5.5 m s^{-1} recorded
 151 between 1983 and 2018. Wind speed shows a clear seasonal variability with average values of 4.0 m s^{-1} in June
 152 and 7.1 m s^{-1} in February (Wawrzyniak and Osuch, 2020). Higher wind speed in winter is attributed to the
 153 increased frequency of extreme cyclonic events in the Arctic (Rinke et al., 2017).

154 3 Methods

155 3.1 Ice mapping

156 The entire archive of Envisat ASAR, RADARSAT-2 and Sentinel-1 synthetic aperture radar (SAR) imagery that
 157 fully covered Hornsund between 2002-10-30 and 2025-08-31 was used in this study (Table 1). The scenes were
 158 geocoded with a pixel size of $50 \times 50\text{ m}$ and an WGS84, UTM33N extent of X: 499-544 km (901 pixels) and Y:
 159 8531-8559 km (561 pixels) until the end of 2023-06 and X: 498.9-549.1 km (1004 pixels), Y: 8530.9-8564.1 km
 160 (664 pixels) starting from 2023-07, a change caused by glacier retreat north- and eastwards beyond the original
 161 area of interest (see Fig. 1). The Envisat ASAR was made up of a single channel (HH or VV) radar backscatter
 162 sigma nought and the incidence angle GeoTIFF rasters created using GASR software (Larsen et al., 2006). For
 163 RADARSAT-2 and Sentinel-1, both HH- and HV-channels radar backscatter sigma nought raster, as well as the
 164 incidence angle information were used.

165

166 **Table 1. Overview of the SAR imagery used in the study.**

Sensor	Start date	End date	Number of images	Number of used images	Image frequency (days)	Binary maps URL
Envisat ASAR	2002-10-30	2012-04-07	1826	1061	3.25	https://doi.org/10.1594/PANGAEA.986427 (Papin et al., 2025a)
RADARSAT-2	2012-01-02	2016-03-01	797	638	2.38	https://doi.pangaea.de/10.1594/PANGAEA.969031 (Swirad et al., 2024b)
Sentinel-1	2014-10-14	2023-06-29	2967	2031	1.57	https://doi.org/10.1594/PANGAEA.963167 (Swirad et al., 2023a) Correction (3 images): https://doi.org/10.5281/zenodo.17350297 (Swirad, 2025)
	2023-07-01	2025-08-31	562	443	1.79	https://doi.org/10.1594/PANGAEA.987853 (Papin et al., 2025b)

167



168 A land mask was created using the Norwegian Polar Institute's land shapefile (NPI, 2014). The land mask was
169 updated for each year on July 1st to account for tidewater glacier retreat and, hence, fjord area increase. Finally,
170 a 100 m buffer was applied to exclude the tidal zone from the analysis (Swirad et al., 2024a).

171

172 To create binary maps of ice and open water, a segmentation algorithm was used. The algorithm was originally
173 developed by Cristea et al. (2020) for open ocean and adapted to the Svalbard fjord environments by Johansson
174 et al. (2020), and to Hornsund by Swirad et al. (2024a). This algorithm is based on a statistical model that accounts
175 for surface-specific intensity decay with increasing incidence angle, a physical property particularly relevant for
176 flat surfaces such as open water and sea ice (Johansson et al., 2020).

177

178 As input, the algorithm requires the incidence angle and one intensity channel, although multiple SAR intensity
179 channels can be used. The HV-channel has lower return power, though is less affected by the wind influence on
180 the water surface which can improve open water vs sea ice separation compared to the HH-channel (Park et al.,
181 2020; Zakhvatkina et al., 2017). However, this channel is limited by a low signal-to-noise ratio (SNR) (Park et
182 al., 2020), and may not always improve the segmentation (Johansson et al., 2020; Zakhvatkina et al., 2017).

183

184 The algorithm is initialized with a single segment, which is iteratively optimized using an Expectation-
185 Maximisation algorithm and evaluated with a Pearson-style goodness-of-fit (GOF) test. If the GOF criterion is
186 not met, the segment is split. In cases where multiple segments exist, the least well-fitting segment is selected for
187 division. This process continues until the algorithm reaches an optimal number of segments, defined as the lowest
188 number that provides a sufficiently good fit to the data. A final contextual smoothing step, based on a Markov
189 Random Field (MRF), is applied to improve spatial coherence and ensure simpler visual interpretation.

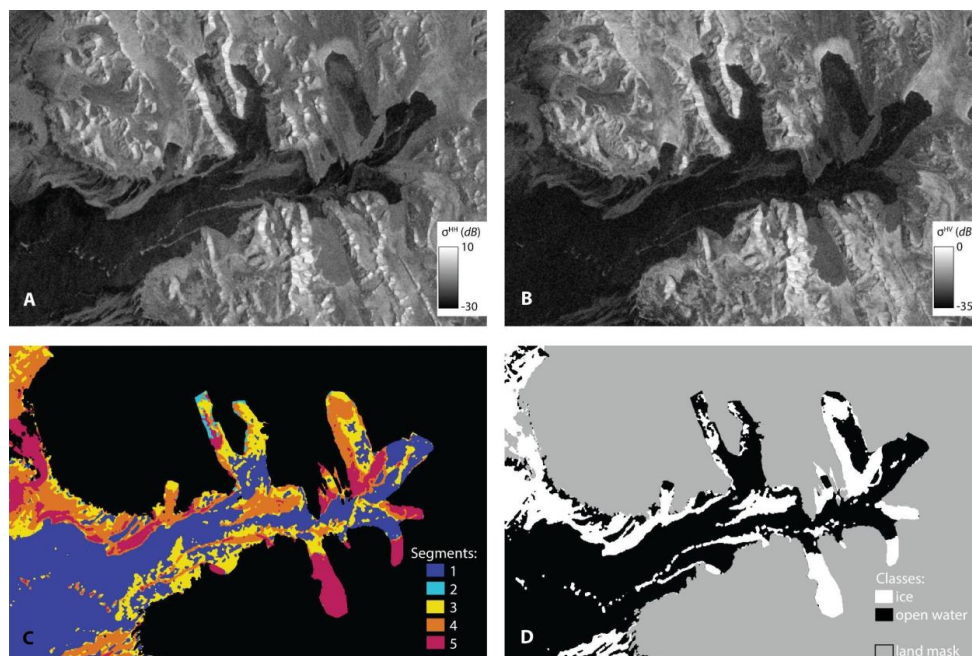
190

191 During the segmentation process, the images were multi-looked 3×3 and log-transformed, and the relevant land
192 mask was used (Johansson et al., 2020; Swirad et al., 2024a). The multi-looked reduced speckle noise and
193 enhanced contrast, while the logarithmic transformation helped approximate a Gaussian distribution of the data
194 (Johansson et al., 2020).

195

196 Typically five (range: 3-6) discontinuous segments were automatically mapped. The segments were then manually
197 classified as either "ice" or "open water" based on user experience and assumptions of (i) a better separation
198 between open water and ice in the HV channel and (ii) a higher backscatter value for ice than open water under
199 calm wind conditions (Johansson et al., 2020; Swirad et al., 2024a). Figure 2 shows an example of an original
200 SAR scene, segmentation and classification.

201



202
203 **Figure 2.** An example of the processing of the Sentinel-1 S1_EWM_20250119_054342_DES_037 scene: (a) HH
204 backscatter intensity, (b) HV backscatter intensity, (c) segmented image, where 1 is the land mask and 2 to 6 are the
205 discontinuous segments, (d) classified image.

206
207 Sentinel-1A/B imagery until 2023-06 was processed by Swirad et al. (2024a), RADARSAT-2 imagery was
208 processed by Swirad et al. (2025). The present study contributed by extending the dataset from 11.5 years to nearly
209 23 years by adding the entire Envisat ASAR archive (Papin et al., 2025a) and Sentinel-1A imagery starting from
210 2023-07 (Papin et al., 2025b), as well as by fixing erroneously processed Sentinel-1 images on 2015-01-18, 2018-
211 12-25 and 2019-02-12 (Swirad, 2025).

212
213 Binary maps were combined into a single time series with a total of 4123 images spanning from 2002-10-30 to
214 2025-08-31, with an average frequency of 2.02 days. Consistency in ice detection between different sensors was
215 previously verified (Johansson et al., 2020; Swirad et al., 2025). When two images occurred on the same day,
216 RADARSAT-2 was prioritised over Envisat ASAR and Sentinel-1 because of its lower noise floor. Validations
217 of the SAR derived maps were carried out by Johansson et al. (2020) through comparisons with GPS tracks of the
218 landfast ice edge and with manually drawn maps from the Zeppelin observatory in Ny-Ålesund, and by Swirad et
219 al. (2024a) through comparisons of the landfast ice edge with 20 temporally and spatially overlapping Sentinel-
220 2 optical images.

221 3.2 Ice analysis

222 Binary ice/open water maps were used to characterise spatial and temporal ice conditions in Hornsund. Ice extent
223 and coverage were calculated for the entire fjord as well as for the main basin and three main bays - Burgerbukta,
224 Brepollen and Samarinvågen as delimited in Fig. 1. The coverage was calculated as the ice extent divided by the



225 area of interest, which was updated annually on July 1st based on the landmask extent varied due to glacier front
226 retreat.

227

228 The first and last day of the presence of drift and landfast ice inside the fjord were found visually in the SAR
229 intensity images and the binary maps. The sea ice season was defined as the period between the first day of drift
230 ice and landfast ice break-up, while the landfast ice season was delimited by the landfast ice freeze-up and break-
231 up. The length of the sea ice and landfast ice seasons, and the average ice coverage during the sea ice and landfast
232 ice seasons were calculated to identify interannual trends. The ice coverage was calculated for the entire fjord and
233 for its parts – the main basin and the three main bays (Fig. 1) – to identify spatial trends. The seasonal analyses
234 start on September 1st which is defined as the sea ice minimum date (Johansson et al., 2020).

235 3.3 Meteorological and oceanographic data

236 Air temperature data from 2002-07-01 to 2025-08-31 come from Vaisala HMP45D and HMP155 probes located
237 2 m above ground level (12 m a.s.l.), near the main buildings of the PPS, approximately 200 m from the shore.
238 The mean hourly temperature was calculated by averaging hourly min and max values, as these two observations
239 were the only ones available until 2008-06. The mean daily air temperature (T) was calculated by averaging the
240 mean hourly temperature. Mean daily wind speed (WS) was averaged from 1 minute data with measurements
241 performed with different instruments at a height of 10 m above the ground (around 20 m a.s.l.). For days with data
242 gaps, the air temperature and wind speed was taken from the dataset provided by Wawrzyniak and Osuch (2020)
243 for all dates before 2019-01-01, and thereafter linear interpolation of up to seven days was applied.

244

245 Daily sea surface temperature (SST) and significant wave height (SWH) outside Hornsund were obtained from
246 ERA5 reanalysis data (Hersbach et al., 2023) for the position 77°N, 15°E at 12:00 UTC from 2002-07-01 to 2025-
247 08-31. Data gaps, which generally overlap with sea ice concentration values over 30%, were left blank.

248

249 T , WS , SST and SWH were subsequently averaged over three months to characterise summer (July-September),
250 autumn (October-December), winter (January-March) and spring (April-June) for each year starting from summer
251 2002. The summer indicates the preceding summer.

252

253 T was also used to calculate the cumulative Freezing Degree Days (FDD) for the period leading to the landfast ice
254 freeze-up and the cumulative Thawing Degree Days (TDD) for the period preceding the landfast ice break-up.
255 FDD represents the sum of the negative temperature on days with degrees below the freezing point of seawater (-
256 1.8°C) starting from Sept 1st, and is defined by the formula given in Equation 1:

257

$$258 FDD = \int_0^t (T_f - T(t)) dt \text{ for } T < T_f \quad (1)$$

259

260 where t is time (days), T_f is the freezing temperature of seawater (°C), and T is the mean daily air temperature
261 (°C).

262



263 Similarly, TDD represents the cumulative sum of degree days with temperatures above 0 °C starting from the
264 landfast ice freeze-up day, and is defined by Equation 2:

265

$$266 \quad TDD = \int_0^t T(t) dt \text{ for } T > T_0 \quad (2)$$

267

268 where T_0 is 0°C, and T is the mean daily air temperature (°C).

269

270 FDD and TDD were also used to estimate the thermodynamically grown landfast ice thickness. To do so, we first
271 calculated the combined effect of FDD and TDD after Su and Wang (2012) as:

272

$$273 \quad \vartheta = FDD - 3 \times TDD \quad (3)$$

274

275 Negative ϑ values were replaced by '0'. We then calculated the ice thickness, SIT (m) using a formula by Lebedev
276 (1938):

277

$$278 \quad SIT = 0.01333 \times \vartheta^{0.58} \quad (4)$$

279

280 The above-mentioned meteorological and oceanographic data were used to (1) characterize conditions during the
281 23 sea ice seasons and identify long-term trends, (2) find relationships (regression) between forcings and ice
282 conditions (season length and ice coverage), and (3) describe environmental conditions leading to the landfast ice
283 freeze-up and break-up.

284 **4 Results**

285 **4.1 Ice conditions over the 23 seasons**

286 The sea ice season began between October and March with the arrival of the drifting ice pack from the southwest,
287 with a mean on December 29th. The landfast ice freeze-up occurred between December and March, with a mean
288 on January 26th. The 2004/05 season had the earliest drift ice arrival (October 27th), followed by the 2019/20
289 season (October 28th), and the 2015/16 season had the latest onset (March 1st). The earliest landfast ice freeze-up
290 occurred in the 2010/11 and 2019/20 (December 18th), and the latest in the 2015/16 (March 30th). The landfast ice
291 freeze-up occurred on average 28 days after the first drift ice, ranging from 0 (2002/03, 2006/07) to 101 (2005/06)
292 days (Table 2). Drift ice was present in the fjord until April-July (average until June 1st), while the landfast ice
293 broke up in May-July (mean on June 24th). The earliest end of both drift ice and landfast ice presence occurred in
294 2013/14 (April 9th and May 19th, respectively), and the latest in 2010/11 (July 20th for both ice types). The landfast
295 ice break-up (end of both the sea ice and the landfast ice seasons) occurred between 0 (2003/04, 2009/10, 2010/11)
296 and 67 (2024/25) days after the last presence of drift ice (average of 23 days). The sea ice season lasted on average
297 178 days, ranging from 105 (2015/16) to 249 (2004/05) days. The landfast ice season lasted on average 150 days,
298 ranging from 61 (2015/16) to 215 (2010/11) days (Table 2).

299



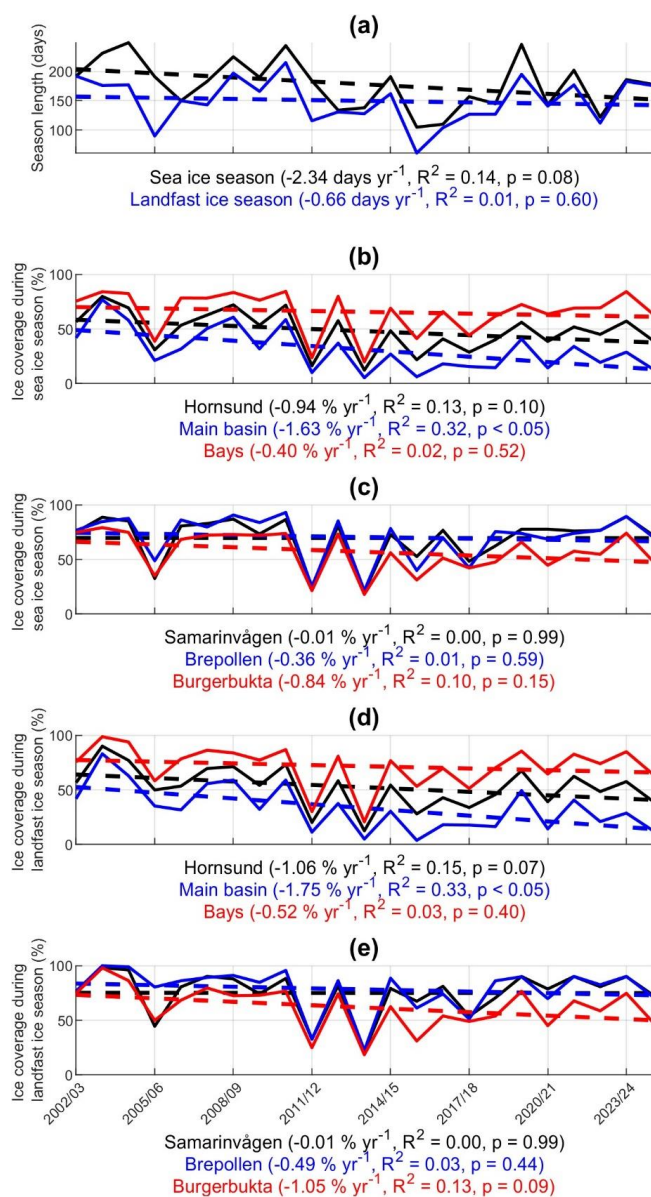
300 **Table 2. The timing and average ice coverage in Hornsund and its parts over the 23 sea ice seasons from 2002-2025.**

Season	First day with drift ice	Landfast ice freeze-up	Last day with drift ice	Landfast ice break-up
2002/03	2 Jan	2 Jan	9 May	12 Jul
2003/04	13 Nov	7 Jan	30 Jun	30 Jun
2004/05	27 Oct	7 Jan	18 Jun	2 Jul
2005/06	3 Dec	14 Mar	10 May	11 Jun
2006/07	31 Jan	31 Jan	26 Apr	29 Jun
2007/08	8 Jan	17 Feb	3 Jul	8 Jul
2008/09	23 Nov	20 Dec	30 May	5 Jul
2009/10	26 Dec	19 Jan	3 Jul	3 Jul
2010/11	19 Nov	18 Dec	20 Jul	20 Jul
2011/12	11 Dec	17 Feb	6 Jun	11 Jun
2012/13	8 Feb	11 Feb	4 Jun	21 Jun
2013/14	2 Jan	12 Jan	9 Apr	19 May
2014/15	29 Dec	27 Jan	13 Jun	7 Jul
2015/16	15 Feb	30 Mar	26 May	29 May
2016/17	1 Mar	7 Mar	18 May	18 Jun
2017/18	30 Dec	29 Jan	23 May	4 Jun
2018/19	25 Jan	12 Feb	3 Jun	18 Jun
2019/20	28 Oct	18 Dec	26 May	29 Jun
2020/21	2 Feb	4 Feb	8 Jun	24 Jun
2021/22	3 Dec	28 Dec	23 May	22 Jun
2022/23	11 Feb	21 Feb	24 May	12 Jun
2023/24	1 Jan	4 Jan	29 Jun	4 Jul
2024/25	10 Jan	12 Jan	30 Apr	6 Jul
Mean	29 Dec	26 Jan	1 Jun	24 Jun

301

302 There was a gradual decrease in the length of the drift ice and landfast ice seasons of 2.34 and 0.66 days yr⁻¹,
 303 respectively, though the relationships are weak and statistically insignificant (Fig. 3a).

304



305
306
307
308
309
310

Figure 3. Time series of ice season parameters in Hornsund over the 23 seasons from 2002-2025: (a) the length of the sea ice season and the landfast ice season; average ice coverage during the sea ice season (b) for the parts of Hornsund, and (c) for individual bays; average ice coverage during the landfast ice season (d) for the parts of Hornsund, and (e) for individual bays.

311
312
313
314
315

The average ice coverage in Hornsund was 48% during the entire sea ice season, but it was higher in the bays (66%) and lower in the main basin (31%). Earlier seasons (2002/03 to 2010/11) experienced higher ice coverage ($\geq 53\%$) with the exception of the 2005/06 (31%). The maximum overall ice coverage was reached in 2003/04 (80% in Hornsund, 77% in the main basin and 84% in the bays). From 2011/12, the average ice coverage was more variable, ranging from 12% in 2013/14 to 57% in 2023/24 (Fig. 4). Of the bays, Brepollen was characterized

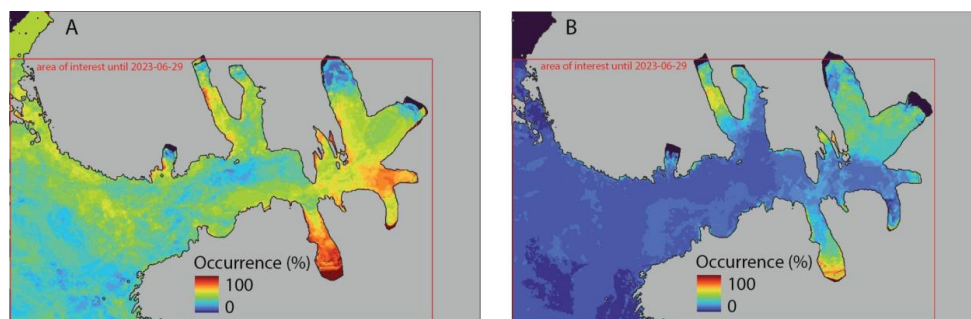


316 by the highest average ice coverage during the sea ice season (70%), followed by Samarinvågen (69%), which
317 had higher ice coverage than Brepollen in some seasons. Meanwhile, Burgerbukta had the lowest average ice
318 coverage during the sea ice season (57%). There was a statistically-significant negative trend in ice coverage in
319 the main basin during the sea ice season ($-1.63\% \text{ yr}^{-1}$, $R^2 = 0.32$, $p < 0.05$). The long-term trends of the entire fjord
320 and the bays were weak and non-significant (Fig. 3b,c).

321
322 The ice coverage during the landfast ice season followed the same interannual and spatial pattern as for the sea
323 ice season. The average coverage was, however, higher by 4, 2 and 6% for Hornsund, main basin and the bays,
324 respectively. The results of linear regression showed a statistically-significant negative trend for the ice coverage
325 in the main basin ($-1.75\% \text{ yr}^{-1}$, $R^2 = 0.33$, $p < 0.05$), while other areas exhibited weak non-significant trends (Fig.
326 3d, e).

327
328 During the landfast ice freeze-up, the drift ice was typically present outside the fjord and in the main basin while
329 landfast ice mostly formed in Samarinvågen and southern Brepollen (Fig. 4a). During the landfast ice break-up
330 the main basin was usually ice-free while the last landfast ice was present in Vestre Burgerbukta, northern
331 Brepollen and depths of Samarinvågen (Fig. 4b).

332



333
334 **Figure 4. Spatial occurrence of ice on the (a) freeze-up and (b) break-up of the landfast ice in Hornsund over the 23**
335 **seasons from 2002–2025.**

336

337 4.2 Meteorological and oceanographic conditions

338 T averaged over the 23 seasons was 4.2°C in summer, -3.6°C in autumn, -8.0°C in winter and -1.7°C in spring.
339 The first negative air temperatures in the fjord occurred between September and November, with the earliest
340 recorded on September 7th (2002) and the latest on November 1st (2016). The last day of negative air temperature
341 occurred between May and June, with the earliest on May 20th (2016 and 2022) and the latest on June 12th (2010).
342 Over the 23 seasons, the minimum T of -28.1°C was recorded on January 13th, 2004, and the maximum of 12.0°C
343 on July 25th, 2020. WS was characterised by a high variability at a daily timescale. Seasonally, stronger winds
344 were observed in winter (6.8 m s^{-1}) and autumn (6.2 m s^{-1}), compared to summer (4.6 m s^{-1}) and spring (5.4 m s^{-1}).
345 The maximum WS of 20.3 m s^{-1} was recorded on January 10th, 2019, while WS of 0 m s^{-1} occurred on 10 days
346 during the study period. SST was the lowest in winter (0.3°C) and the highest in summer (4.2°C). It averaged
347 1.2°C in autumn and 0.9°C in spring. The first negative SST values occurred between October and March, with
348 the earliest recorded on October 17th (2005) and the latest on March 28th (2017). The last day with negative SST

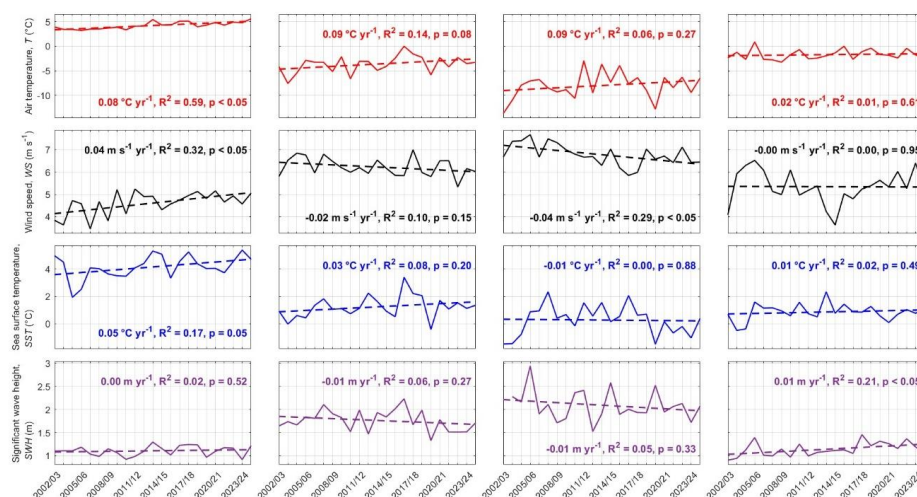


349 occurred between April and July, with the earliest on April 1st (2006) and the latest on July 7th (2004). Over the
 350 23 seasons, the lowest *SST* of -1.8°C was recorded on April 27th, 2013, and the highest of 7.4°C on August 14th
 351 and 15th, 2002. *SWH* was the highest in winter (2.1 m), followed by autumn (1.8 m), spring (1.1 m), and summer
 352 (1.1 m). The largest *SWH* of 7.9 m was observed on February 7th, 2025, and the lowest of 0.2 m occurred on July
 353 7th, 2003, May 19th, 2020, and May 4th, 2021.

354

355 There was a strong statistically-significant trend of increasing T_{summer} over the analysed 23 seasons ($+0.08^{\circ}\text{C yr}^{-1}$,
 356 $R^2 = 0.59$, $p < 0.05$). The other seasons also experienced a gradual T increase, but relationships are weak and non-
 357 significant. WS increased in summer ($+0.04\text{ m s}^{-1}\text{ yr}^{-1}$, $R^2 = 0.32$, $p < 0.05$) and decreased in winter ($-0.04\text{ m s}^{-1}\text{ yr}^{-1}$,
 358 $R^2 = 0.29$, $p < 0.05$). Trends in autumn and spring were weak and non-significant. *SST* trends were generally
 359 weaker than those observed for T with the summer increase of $+0.05^{\circ}\text{C yr}^{-1}$ ($R^2 = 0.17$, $p = 0.05$) and a negligible
 360 and non-significant trends in other seasons. *SWH* exhibited a limited long-term changes across seasons with the
 361 only statistically-significant positive trend in spring ($+0.01\text{ m yr}^{-1}$, $R^2 = 0.21$, $p < 0.05$) (Fig. 5).

362



363

364 **Figure 5. Seasonal averages of meteorological and oceanographic parameters in Hornsund for the 23 seasons from**
 365 **2002-2025.**

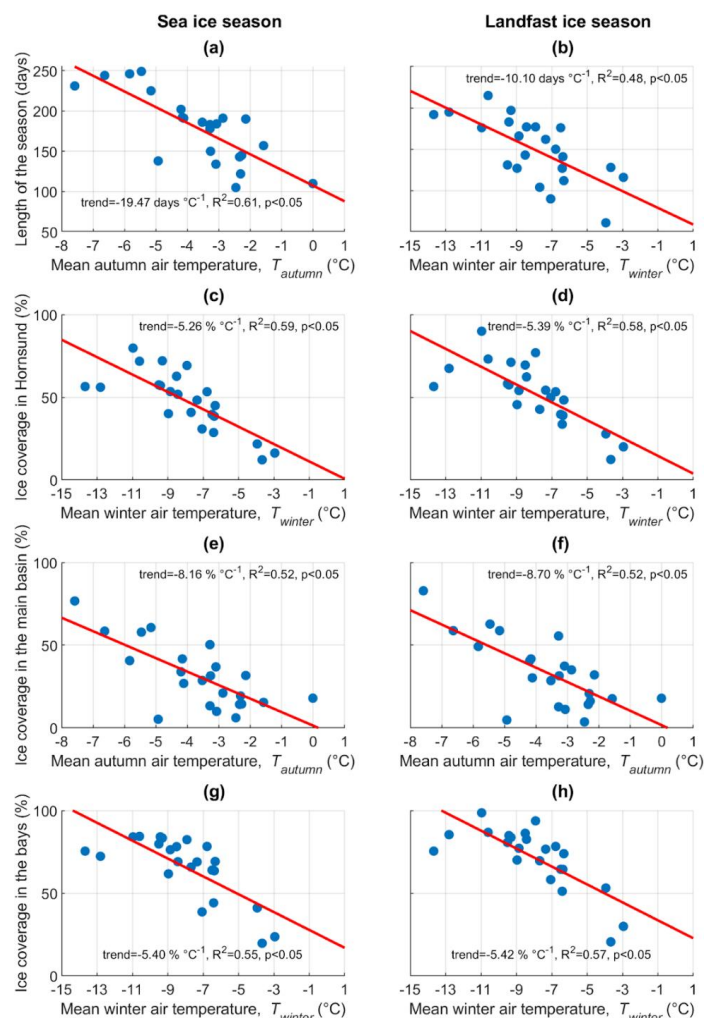
366

367 4.3 Relationships between environmental conditions and the ice-season parameters

368 In general, longer and icier seasons were associated with colder autumns and winters. The 2003/04 season had the
 369 highest ice coverage in Hornsund (80% during the sea ice and 90% during the landfast ice season), the lowest
 370 T_{autumn} (-7.6°C), the third lowest T_{winter} (-11.0°C), one of the highest WS_{winter} (7.4 m s^{-1}), the lowest SST_{spring} (-
 371 0.5°C). The 2004/05 season had the longest sea ice season (249 days), the second-highest ice coverage in the fjord
 372 during the landfast ice season (77%), and the earliest first drift ice (October 27th). It was characterized by the
 373 lowest SST_{summer} (1.9°C) and one of the highest WS_{winter} (7.4 m s^{-1}). The 2010/11 season had the longest landfast
 374 ice season (215 days) related to the earliest landfast ice freeze-up (December 18th) and the latest landfast ice break-
 375 up (July 20th). T_{summer} was the second lowest (3.3°C), and T_{winter} was one of the lowest (-10.6°C). The 2019/20



376 season also had the earliest landfast ice onset (December 18th). Additionally, it had also one of the largest ice
377 coverages, particularly in the bays (72% during sea ice season and 85% during landfast ice season). It was
378 characterized by the lowest SST_{winter} (-1.5°C), the lowest SST_{autumn} (-0.4°C), and the lowest SWH_{autumn} (1.3 m).
379 The 2013/14 season had the lowest ice coverage in Hornsund (12% during both the sea ice and the landfast ice
380 seasons) and its bays (20% during the sea ice and 21% during the landfast ice season), and the earliest end of the
381 landfast ice season (May 19th). This season had the highest SST_{spring} (2.3°C), the highest SWH_{summer} (1.3 m) and
382 the second highest T_{winter} (-3.7°C). The 2015/16 season had the shortest sea ice and landfast ice seasons (105 and
383 61 days, respectively), the latest landfast ice onset (March 30th), and the lowest ice coverage in the main basin
384 (3.6%). This season was marked by the second highest T_{spring} (-3.2°C). The 2016/17 season had the latest
385 occurrence of the first drift ice (March 1st). It was also characterized by the highest T_{autumn} (-0.01°C) and the lowest
386 WS_{winter} (5.9 m s^{-1}) and it recorded the highest SST_{autumn} (3.4°C), as well as the highest SWH_{autumn} (2.2 m).
387
388 Strong ($R^2 \geq 0.48$) statistically-significant ($p < 0.05$) negative relationships exist between T_{autumn} or T_{winter} and all
389 considered characteristics of sea ice and landfast ice seasons: season length and ice coverage in Hornsund, the
390 main basin and the bays (Fig. 6). The length of the sea ice season decreased by 19.5 days per 1°C increase in
391 T_{autumn} ($R^2 = 0.61$, $p < 0.05$), while the length of the landfast ice season decreased by 10.1 days per 1°C increase
392 in T_{winter} ($R^2 = 0.48$, $p < 0.05$). The average ice coverage in the main basin during the sea ice season decreased by
393 8.2% per 1°C increase in T_{autumn} ($R^2 = 0.52$, $p < 0.05$). The ice coverage the entire fjord and in the bays during the
394 sea ice season depended on the T_{winter} with trends of -5.3% per 1°C ($R^2 = 0.59$, $p < 0.05$) and -5.4% per 1°C ($R^2 =$
395 0.55 , $p < 0.05$), respectively. Similar patterns were observed for the ice coverage during the landfast ice season
396 with the respective trends of -5.4% per 1°C ($R^2 = 0.58$, $p < 0.05$), 8.7% per 1°C ($R^2 = 0.52$, $p < 0.05$) and 5.4%
397 per 1°C ($R^2 = 0.57$, $p < 0.05$) in Hornsund, the main basin and the bays, respectively (Fig. 6).
398



399

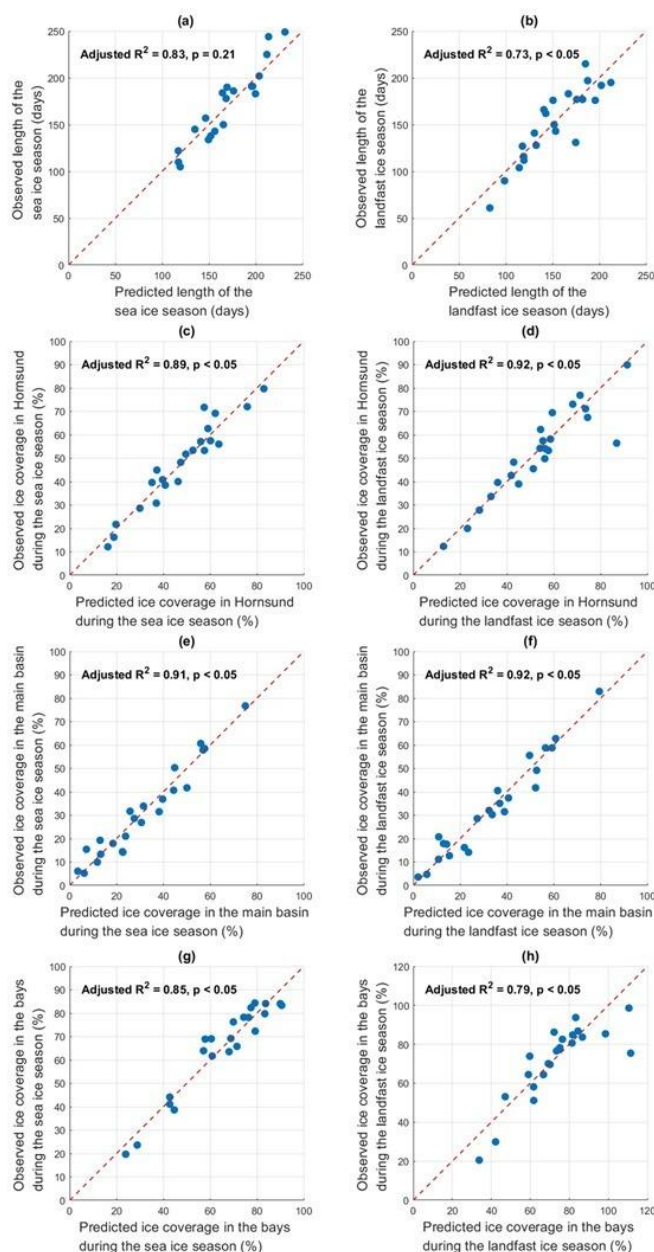
400 **Figure 6. Linear correlations between the highest-correlation environmental driver (mean autumn or winter air**
 401 **temperature) and the ice-season parameters over the 23 seasons from 2002-2025: (a-b) length of the season; (c-d)**
 402 **average ice coverage in Hornsund; (e-f) average ice coverage in the main basin; (g-h) average ice coverage in the bays.**
 403 **The left panel represents the sea ice season and the right panel – the landfast ice season.**

404

405 Figure 7 shows results of the linear stepwise regression models relating environmental drivers to key parameters
 406 of the sea ice season (left panel) and the landfast ice season (right panel). The 16 drivers (T , WS , SST and SWH
 407 over summer, autumn, winter and spring) were considered. For all ice-season parameters using multiple predictors
 408 improved the fit (adjusted $R^2 \geq 0.73$, $p < 0.05$ for seven out of eight parameters) compared to a single predictor
 409 (Fig. 7). T_{winter} appears in all eight ice-season parameters and is consistently associated with a negative
 410 relationship. T_{autumn} and T_{spring} explain four parameters, and in all cases their relationship with the ice-season
 411 parameters is negative. T_{summer} represents an outlier, as it appears only in the equation for the average ice coverage
 412 in the bays during the sea ice season, where it shows a positive relationship. WS_{summer} appears in six cases and is



413 consistently associated with a negative relationship. In contrast, WS_{winter} is present in five of the ice-season
414 parameters and always shows a positive relationship. WS_{autumn} appears in three cases, with a positive relationship
415 in two of them (the length of the sea ice season and the average ice coverage in the main basin during the landfast
416 ice season), and a negative relationship in the average ice coverage in the bays during the sea ice season. WS_{spring}
417 does not appear in any of the equations. SST_{spring} is present in six out of eight cases and is consistently associated
418 with a negative relationship. $SST_{winters}$, which appears in the equations for the average ice coverage in the main
419 basin during both the sea ice and landfast ice seasons, shows a positive relationship. SST_{autumn} also exhibits a
420 positive relationship for the average ice coverage in the main basin and in the bays during the sea ice season, but
421 a negative relationship for the length of the sea ice season. SST_{summer} , which is present in half of the cases, always
422 has a negative correlation. SWH_{summer} and SWH_{autumn} each appear in two cases and are consistently associated with
423 a negative relationship. SWH_{winter} is present in three cases, showing a negative relationship in two of them (the
424 average ice coverage in Hornsund and in the bays during the sea ice season), and a positive relationship for the
425 length of the sea ice season. Finally, SWH_{spring} does not appear in any of the equations (Table 3).



426

427 **Figure 7. Results of the stepwise regression between environmental drivers and ice-season parameters over the 23**
428 **seasons from 2002-2025: (a-b) length of the season; (c-d) average ice coverage in Hornsund; (e-f) average ice coverage**
429 **in the main basin; (g-h) average ice coverage in the bays. The left panel represents the sea ice season and the right panel**
430 **– the landfast ice season.**

431



432 **Table 3. Stepwise regression models of the ice-season parameters in Hornsund over the 23 seasons from 2002-2025.**

Ice-season parameter	Best-fit model	Adjusted R ²	p-value
Length of the sea ice season	$-135.76 - 5.09 \times T_{\text{autumn}} - 7.14 \times T_{\text{winter}} - 12.74 \times T_{\text{spring}} + 26.16 \times WS_{\text{autumn}} - 18.63 \times SST_{\text{autumn}} + 37.28 \times SWH_{\text{winter}}$	0.83	0.21
Average ice coverage in Hornsund during the sea ice season	$9.98 - 4.43 \times T_{\text{winter}} - 2.60 \times T_{\text{spring}} - 10.72 \times WS_{\text{summer}} + 10.45 \times WS_{\text{winter}} - 5.07 \times SST_{\text{spring}} - 8.51 \times SWH_{\text{winter}}$	0.89	7.04×10^{-6}
Average ice coverage in the main basin during the sea ice season	$23.63 - 6.31 \times T_{\text{autumn}} - 3.11 \times T_{\text{winter}} - 10.22 \times WS_{\text{summer}} + 5.82 \times WS_{\text{winter}} - 3.90 \times SST_{\text{summer}} + 7.23 \times SST_{\text{autumn}} + 3.30 \times SST_{\text{winter}} - 9.09 \times SST_{\text{spring}} - 16.42 \times SWH_{\text{summer}}$	0.91	4.80×10^{-4}
Average ice coverage in the bays during the sea ice season	$66.60 + 15.83 \times T_{\text{summer}} - 5.11 \times T_{\text{winter}} - 17.75 \times WS_{\text{summer}} - 5.56 \times WS_{\text{autumn}} + 17.79 \times WS_{\text{winter}} - 7.09 \times SST_{\text{summer}} + 8.37 \times SST_{\text{autumn}} - 7.12 \times SST_{\text{spring}} - 56.25 \times SWH_{\text{summer}} - 11.61 \times SWH_{\text{winter}}$	0.85	0.03
Length of the landfast ice season	$108.31 - 8.51 \times T_{\text{autumn}} - 5.97 \times T_{\text{winter}} - 14.18 \times T_{\text{spring}} - 34.71 \times SWH_{\text{autumn}}$	0.73	8.68×10^{-3}
Average ice coverage in Hornsund during the landfast ice season	$25.92 - 4.70 \times T_{\text{winter}} - 10.82 \times WS_{\text{summer}} + 8.32 \times WS_{\text{winter}} - 2.54 \times SST_{\text{summer}} - 6.84 \times SST_{\text{spring}}$	0.92	4.48×10^{-7}
Average ice coverage in the main basin during the landfast ice season	$-3.08 - 4.43 \times T_{\text{autumn}} - 4.13 \times T_{\text{winter}} - 10.75 \times WS_{\text{summer}} + 5.84 \times WS_{\text{autumn}} + 6.24 \times WS_{\text{winter}} - 3.23 \times SST_{\text{summer}} + 7.42 \times SST_{\text{winter}} - 10.11 \times SST_{\text{spring}} - 12.16 \times SWH_{\text{autumn}}$	0.92	3.66×10^{-3}
Average ice coverage in the bays during the landfast ice season	$84.21 - 5.16 \times T_{\text{winter}} - 9.58 \times WS_{\text{summer}} - 9.51 \times SST_{\text{spring}}$	0.79	3.00×10^{-5}

433

434 **4.4 Conditions leading to the landfast ice freeze-up and break-up**

435 In the period leading to the onset of landfast ice, T gradually decreased ($-0.1^\circ\text{C day}^{-1}$, $R^2 = 0.81$, $p < 0.05$) with
 436 the average below the sea water freezing point for > 90 days (Fig. 8a). The 2009/10 season had the highest T ($-$
 437 3.1°C), while the 2003/04 season had the lowest T during this 90-days period (-8.2°C). The drift ice appeared on
 438 average 28 days earlier, ranging from 0 (2002/03 and 2006/07) and 101 days (2005/06). Ice coverage during the
 439 period between first drift and landfast ice averaged 21% with the minimum of 0% in 2009/10 (drift ice was present
 440 outside the fjord and no imagery was available between December 26th and January 19th for a better assessment)
 441 and the maximum of 85% in 2008/09 (Table 4). Ice coverage generally remained low during the early part,
 442 followed by an increase as the landfast ice freeze-up approached. The timing varied from year to year but 40 days
 443 before the landfast ice freeze-up the average ice coverage exceeded 20%. The average coverage of 26%
 444 characterised the day before and 46% the freeze-up day (Fig. 9). The period leading to the landfast ice freeze-up
 445 was also characterised by the gradual decrease of SST ($-0.02^\circ\text{C day}^{-1}$, $R^2 = 0.89$, $p < 0.05$) and an increase of WS
 446 ($+0.02 \text{ m s}^{-1} \text{ day}^{-1}$, $R^2 = 0.31$, $p < 0.05$) and SWH ($+0.004 \text{ m day}^{-1}$, $R^2 = 0.21$, $p < 0.05$) (Fig. 8 c, e, g). The average
 447 number of consecutive days with T below the freezing point was 9.7, but the difference between FDD over
 448 consecutive days with $T < 1.8^\circ\text{C}$ (79°C days) and the ϑ over the entire period from the first day with $T < 1.8^\circ\text{C}$
 449 (268°C days) suggests T oscillation around the freezing point (Table 4).

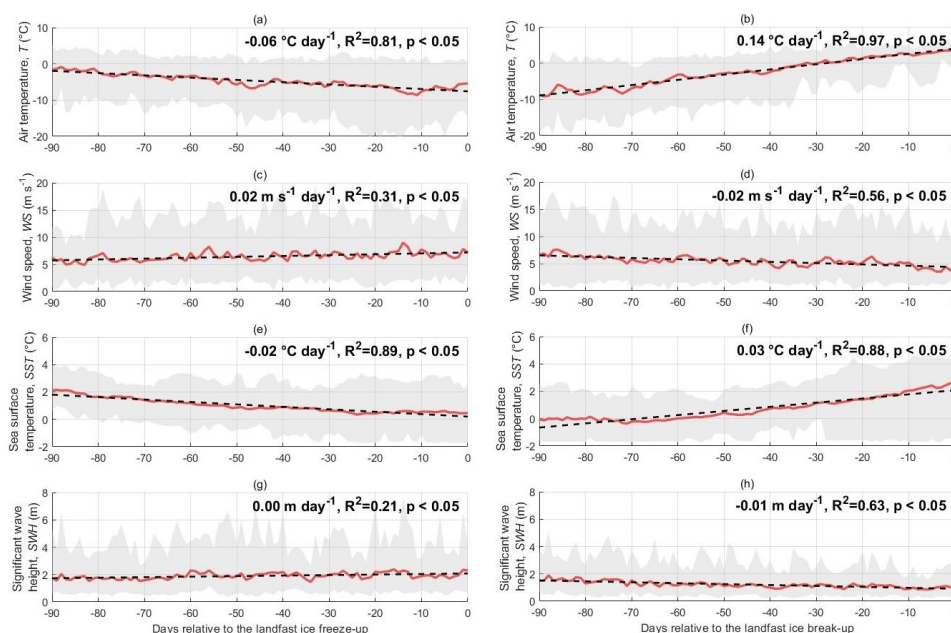
450



451 Table 4. Conditions leading to the landfast ice freeze-up and break-up in Hornsund.

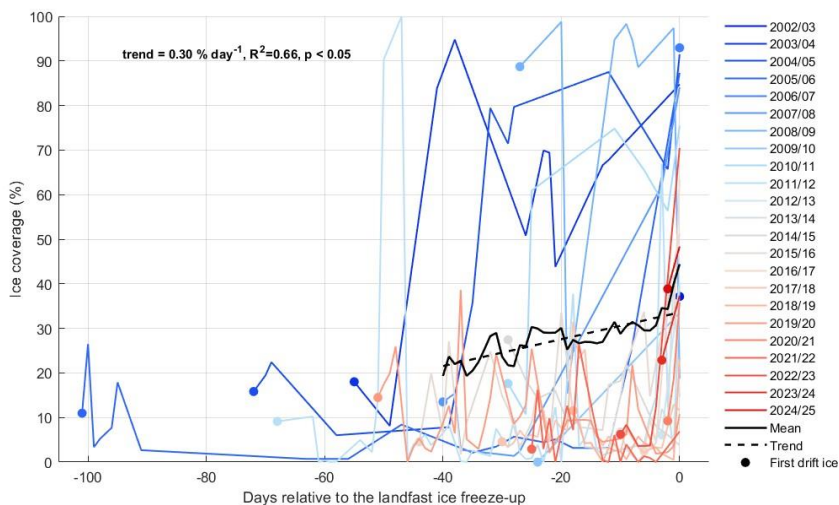
Season	Landfast ice freeze-up						Landfast ice break-up			
	Number of days with drift ice	Average ice coverage (%)	Number of consecutive days with $T < -1.8^{\circ}\text{C}$	FDD on the day ($^{\circ}\text{C days}$)	$\bar{\theta}$ on the day ($^{\circ}\text{C days}$)	Thermod ynamic ice thickness (m)	Number of consecutive days with $T > 0^{\circ}\text{C}$	TDD on the day ($^{\circ}\text{C days}$)	$\bar{\theta}$ on the day ($^{\circ}\text{C days}$)	Thermod ynamic ice thickness (m)
2002/03	0	NoValue	24	195	185	0.27	41	120	1067	0.76
2003/04	55	57	34	446	560	0.52	22	45	1296	0.85
2004/05	72	45	6	35	398	0.43	30	70	912	0.69
2005/06	101	7.6	20	197	389	0.42	12	39	357	0.40
2006/07	0	NoValue	20	167	295	0.36	30	80	565	0.52
2007/08	40	16	6	35	325	0.38	29	89	696	0.59
2008/09	27	85	1	7.3	246	0.32	30	105	969	0.72
2009/10	24	0	0	0	130	0.22	20	56	616	0.55
2010/11	29	48	0	0	392	0.42	53	182	823	0.65
2011/12	68	11	7	49	149	0.24	0	0	403	0.43
2012/13	3	6.1	1	0	275	0.35	23	59	851	0.67
2013/14	10	9.9	0	0	366	0.41	0	0	711	0.60
2014/15	29	13	2	17	232	0.31	36	121	430	0.45
2015/16	44	14	1	0.9	206	0.29	8	20	213	0.30
2016/17	6	16	22	160	265	0.34	16	51	546	0.51
2017/18	30	8.2	4	20	158	0.25	12	22	557	0.52
2018/19	18	3.8	7	32	231	0.31	21	62	531	0.51
2019/20	51	10	12	99	306	0.37	38	107	1249	0.83
2020/21	2	14	24	144	217	0.30	28	62	470	0.47
2021/22	25	6.1	9	68	279	0.35	32	108	851	0.67
2022/23	10	6.8	4	32	194	0.28	14	30	483	0.48
2023/24	3	23	3	26	202	0.29	37	123	689	0.59
2024/25	2	39	16	94	164	0.26	41	124	373	0.41
Mean	28	21	9.7	79	268	0.33	25	73	681	0.57

452



453

454 **Figure 8.** Evolution of (a-b) air temperature, T , (c-d) wind speed, WS , (e-f) sea surface temperature, SST , and (g-h)
 455 significant wave height, SWH , 90 days before the landfast ice freeze-up (left side) and break-up (right side) in Hornsund
 456 over the 23 seasons from 2002-2025.



457

458 **Figure 9.** Ice coverage in Hornsund from the first drift ice to the landfast ice freeze-up over the 23 seasons from 2002-
 459 2025.

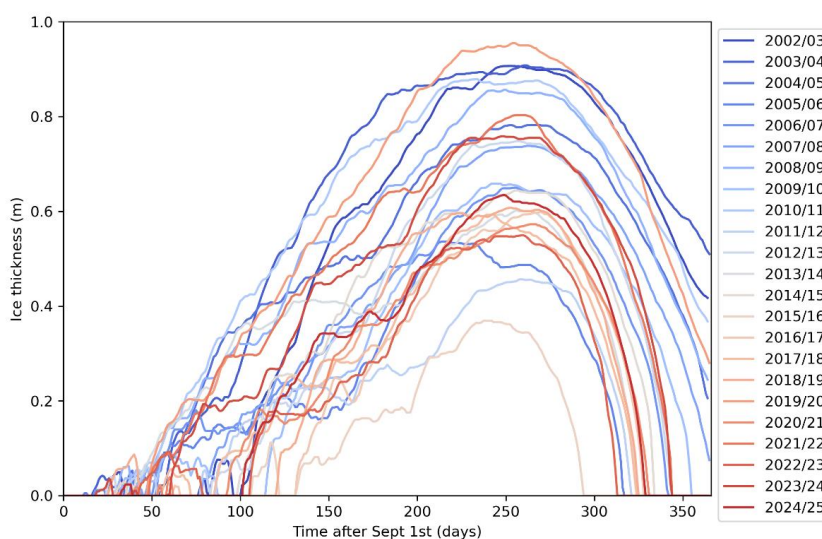
460



461 In the period leading to the landfast ice break-up T grew gradually ($+0.1^{\circ}\text{C day}^{-1}$, $R^2 = 0.97$, $p < 0.05$), exceeding
462 0°C on average 38 days before the last day with landfast ice (Fig. 14b). The number of consecutive days with
463 positive T varied from 0 (2011/12 and 2013/14) to 53 (2010/11) with the average of 25 days, which resulted in
464 the TDD of 73°C days on the last day with the landfast ice (Table 4). There was also a gradual decrease in WS ($-$
465 $0.02\text{ m s}^{-1}\text{ day}^{-1}$, $R^2 = 0.81$, $p < 0.05$) and SWH (-0.01 m day^{-1} , $R^2 = 0.63$, $p < 0.05$), and an increase in SST ($+0.03^{\circ}\text{C}$
466 day^{-1} , $R^2 = 0.88$, $p < 0.05$) over 90 days leading to the landfast ice break-up (Fig. 8d,f,h).

467 4.5 Sea ice thickness

468 Calculation of sea ice thickness thermodynamic growth shows a large variability between the seasons (Fig. 10).
469 In most seasons the ice formation started a few times with T oscillation around the freezing and melting points in
470 autumn. In general, the earlier the start of ice growth the larger the maximal thickness and the longer the sea ice
471 season. The largest thickness of 0.96 m was reached in the 2019/20 season, followed by the 0.91 m in the first two
472 seasons. The smallest thickness was observed in 2015/16 (0.37 m) and 2011/12 (0.46 m). For seven seasons the
473 calculated thickness on August 31st was still positive despite the latest landfast ice break-up on July 20th (Fig. 10).
474 The estimated ice thickness on the day when we visually established the landfast ice freeze-up in the SAR imagery
475 and the binary maps averaged 0.33 m ranging from 0.22 to 0.52 m, and on the landfast ice break-up it was on
476 average 0.57 m with the range of 0.30-0.85 m (Table 4).



477

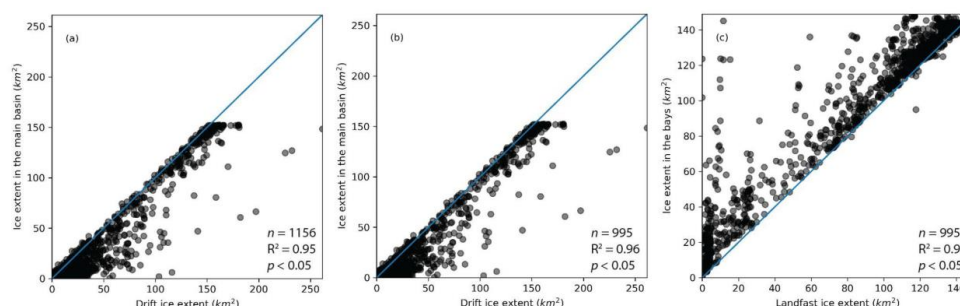
478 **Figure 10. Time series of sea ice thickness in Hornsund calculated using the method of Su and Wang (2012) for the 23**
479 **seasons from 2002-2025.**

480 5 Discussion

481 This study is the third of a series of articles that focus on sea ice conditions in the Hornsund fjord, Svalbard. The
482 first publication (Swirad et al., 2024a) adapted a semi-automated method of Cristea et al. (2020) and Johansson
483 et al. (2020) to create high-resolution (50 m) near-daily binary maps of ice and open water of Hornsund using the



484 full Sentinel-1A/B archive available at the time. The main findings included (1) a large interannual variability in
 485 sea ice conditions without a clear trend over the nine analysed seasons, (2) differences in timing and extent of the
 486 ice cover in different parts of the fjord, notably the main basin and the inner bays, and (3) a presence of a secondary
 487 peak in ice coverage in the bays in autumn, that the authors attributed to the presence of glacier ice (Swirad et al.,
 488 2024a). The second study (Swirad et al., 2026b) expanded the dataset back in time to include the full
 489 RADARSAT-2 archive and developed a method to separate the ice into glacier ice, drift ice and landfast ice. The
 490 authors showed that the ice in Hornsund was 53% drift, 35% landfast, 8.5% glacier ice, while the remaining 3.5%
 491 was either unclassified or masked out. Statistically-significant negative relationships were found between winter
 492 (January-March) water temperature and the length of the sea ice and landfast ice seasons, and between winter air
 493 temperature and the mean coverage of sea ice (drift and landfast ice combined) and landfast ice. Glacier ice
 494 coverage was negatively correlated with summer air and autumn water temperatures. At the 12-season scale no
 495 long-term trends in ice conditions were detected (Swirad et al. 2026b). In this study we further extended the dataset
 496 in time – backward by using the full Envisat ASAR archive (Papin et al., 2025a) and forward by using subsequent
 497 Sentinel-1A imagery (Papin et al., 2025b). We supplemented the dataset with meteorological data from the PPS
 498 monitoring programme, and oceanographic data from ERA5 reanalysis for a location outside the fjord. Because
 499 of the strong ($R^2 = 0.95-0.96$) statistically-significant ($p < 0.05$) relationships between the extent of drift ice from
 500 Swirad et al. (2026b) and our ice extent in the main basin for both the sea ice and the landfast ice seasons, as well
 501 as between the landfast ice from Swirad et al. (2026b) and our ice extent in the bays (Fig. 11), we treat the
 502 differences between the main basin vs the bays as a proxy for the differences between drift vs landfast ice.
 503



504

505 **Figure 11. Spatial extent of the drift and landfast ice in Hornsund from Swirad et al. (2026b) and the ice extent in the**
 506 **main basin and the bays from our study on individual days between 2012-01-02 and 2023-06-29.**

507

508 Expanding the dataset to 23 seasons allowed us to observe the expected long-term decreasing trends in the length
 509 of ice season and in ice coverage, such as those observed by Onarheim et al. (2014), Dahlke et al. (2020) and
 510 Stocker et al. (2020). The trends are stronger for the sea ice season compared to the landfast ice season, and for
 511 the main basin compared to the bays (Fig. 3). This suggests that mostly the pack ice is affected, as generally in
 512 the Arctic, while the state of the landfast ice may be more affected by local conditions, such as those of sheltered
 513 bays of eastern Hornsund. Notably, the variability of season length was more dependent on the start of the season
 514 (October-March) than on its end (May-July). The start of sea ice season is associated with the arrival of pack ice



515 from the Barents Sea, while the end represents the disappearance of landfast ice. The unstable start vs the stable
516 end of the sea ice season further confirms that the drift ice is mostly affected. Arażny et al. (2018) observed a
517 gradient in meteorological conditions (temperature and humidity) between the more maritime western and more
518 continental eastern Hornsund. The Atlantification of Hornsund where the warmer and more saline Atlantic Water
519 becomes dominant over the cooler and fresher Arctic Water (Strzelewicz et al., 2021) affects mostly the outer
520 parts of Hornsund, while the inner bays remain highly affected by glacier outflow (Korhonen et al., 2024).

521

522 The decline of pack ice drifting to the entrance of Hornsund from the Barents Sea was also shown by Herman et
523 al. (2025) for the 1979-2023 ERA5 reanalysis data, though the authors pointed to a ‘regime shift’ after 2005 rather
524 than a gradual change. A decline of the sea ice in Hornsund was also shown by Muckenhuber et al. (2016) on the
525 2000-2014 optical and SAR imagery, though they identified icy periods of 2000-2005 and 2009-2011, and non-
526 icy periods of 2006-2008 and 2012-2014, which could alternatively suggest warmer and colder periods of ~three
527 years. Of the bays, Burgerbukta experienced the fastest decline of the ice coverage during the sea ice and landfast
528 ice seasons, which is intuitive given its location in northern Hornsund, most exposed to the waves arriving from
529 the south-west (Herman et al., 2019; Swirad et al., 2023b). We observed a gradual increase in air and water
530 temperatures, particularly in autumn months (Fig. 5), which could decrease persistence (increase melting) of drift
531 ice, as well as delay the in situ ice formation. Interestingly, there is a statistically-significant decline in winter
532 wind speed. Wind at the beginning of the sea ice season may accelerate ice production through deformation
533 (Kwok, 2006). This phenomenon may become limited with decreasing wind speed, further contributing to slower
534 in situ ice production.

535

536 On the top of the general trend of ice decline, there is a great variability in ice conditions from year to year that
537 was already noticed in our previous studies (Swirad et al., 2024a; 2026b). The longest sea ice seasons and the
538 largest ice coverage characterised the first three seasons (pre-regime shift) as well as two late seasons of 2019/20
539 and 2021/22. Conversely, the 2011/12 and 2013/14 remain the least icy seasons of the 21st century, while the
540 2015/16 was the shortest (Table 2). The seasonal ice parameters are strongly (R^2 of 0.48-0.61) correlated to T_{autumn}
541 and T_{winter} (Fig. 6). T_{autumn} plays a major role for the length of the sea ice season and the ice coverage in the main
542 basin during both the sea ice and landfast ice seasons, further pointing to the variability of drift ice conditions at
543 the beginning of the season. Conversely, the length of the landfast ice season as well as the ice coverage in the
544 bays respond mostly to T_{winter} , which is the period of landfast ice formation. T in the winter months through FDD
545 widely controls ice thickness increase which then affects the time needed to melt/break-up the landfast ice at the
546 end of the season. We found that all ice season parameters correlated better with T than water temperature. This
547 result is different from that of our previous study (Swirad et al., 2026b), in which water temperature controlled
548 the length of the season, and air temperature - ice coverage. We ascribe this difference to the duration of the study
549 (23 vs 12 seasons) as well as using SST of a point outside Hornsund (here) and sea bed mooring data at 10-23 m
550 depth (previous study). De Steur et al. (2023) found a relationship between Fram Strait ice extent and water
551 temperature measured at 55-2440 m depths. However, no in situ water temperature data were available for the
552 entire 2002-2025 period of this study and ERA5 reanalysis was used instead.

553



554 Multiple linear regression showed that combining multiple parameters allows a better fit (R^2 of 0.73-0.92) between
555 the environmental and the eight ice season parameters than using a single variable (Fig. 7). T_{autumn} and T_{winter} were
556 still the most important, but other parameters were also included (Table 3). The impact of SST was similar though
557 weaker than the air temperature. For six ice parameters, WS_{summer} was important, showing a negative correlation,
558 though the physical meaning seems unclear. The positive relationship between WS_{autumn} and the length of the sea
559 ice season supports the acceleration of ice production through deformation (Kwok, 2006). We did not find any
560 negative relationships between WS_{spring} and/or SWH_{spring} and ice season parameters to support the hypothesis of
561 faster landfast ice break-up and melting by wind waves (Graham et al., 2019). SWH was generally the least
562 important factor, which we justify by wave transformation at the entrance and inside the fjord which prevents
563 direct comparison between the value from a single point outside the fjord and ice conditions in the fjord itself.
564 However, when present, the relationship was negative which supports that waves break ice contributing to the
565 shortening of the season and decrease of ice extent (Table 3). Long-term monitoring of water temperature and
566 wave parameters could allow for more direct relationships to be identified.

567

568 We also observed a temporal shift in ice phenomena over the years. The first seasons (pre-regime shift, 2005)
569 were characterised by a rapid increase in ice coverage between December and January, later it was from January
570 to February, and in some years from February to March (Fig. S3 in the Supplement). In consequence, Hornsund
571 shores are more exposed to storm waves, and the hazard of coastal flooding and erosion is higher. Zagórski et al.
572 (2015) pointed to autumn as a season of limited ice cover and large waves. However, our results suggest that
573 December-February may be critical months, both because it is the season with the most intense storms (Swirad et
574 al., 2023b) and because it experiences significant ice decline. Glacier calving and glacier ice accumulation in the
575 bays, despite glacier retreat between June and October-December (Błaszczuk et al., 2023), may not level this shift.
576 Glacier ice tends to be spread or grouped in belts, and it does not attenuate wave energy as efficiently as sea ice;
577 it may also serve as abrasive tool, e.g. when moving up and down the shore with waves (Swirad et al., 2026a).
578 Swirad et al. (2026b) observed a negative correlation between glacier ice coverage and both the glacier calving
579 (approximated by the increase of annual land mask) and the summer air and autumn water temperatures, which
580 suggests that although fewer growlers and bergy bits are expelled from glacier fronts during cold
581 summers/autumns, they persist in the fjord for longer. Li et al. (2025) observed that for southern Svalbard the
582 peak in air temperature occurred in late June, followed by a peak in water temperatures in August and a peak in
583 glacier retreat in September, showing a clear trend between the water temperatures and the glacier retreats.

584

585 Suitable conditions for the landfast ice formation include the presence of drift ice (Figs. 4 and 9) that attenuates
586 waves and lowers near-surface water temperature, and extended period of cold air temperatures. As temperatures
587 may return to the melting point a few times before the landfast ice onset, ϑ , the cumulative effect of FDD and
588 TDD starting from the first day below -1.8°C , seems to better reflect conditions necessary for water freezing than
589 the number of consecutive days with negative temperatures or TDD over these (both can be 0). The minimal ϑ on
590 the day of the landfast ice freeze-up was 130°C days (Table 4). The ice thickness calculated in thermodynamic
591 terms (Lebedev, 1938) for the landfast ice freeze-up day was on average 0.33 m, which may indicate a minimum
592 thickness needed for ice detection using C-band SAR imagery. New SAR missions, the recently launched NISAR
593 (NASA-ISRO) mission and upcoming ROSE-L (ESA), are carrying the L-band sensors with the free and open



594 data policy, and in early March 2026 there were already approx. 180 NISAR images collected over Hornsund.
 595 Wakabayashi et al. (2004) showed a relationship between the L-band SAR backscatter values and sea ice thickness
 596 from approx. 5-10 cm thickness. For earlier years, it is possible that the landfast ice onset could be visible on SAR
 597 imagery earlier but the lower temporal resolution of Envisat ASAR imagery resulted in a less accurate start date
 598 for the freeze-up. However, the seasons with the largest data gap before the landfast ice onset represented both
 599 thinner (2009/10, 2002/03) and thicker (2003/04) than average ice (Table 5).

600

601 **Table 5. Dates and number of days with no data before/after the landfast ice freeze-up/break-up in Hornsund.**

Season	Number of days with no data before landfast ice freeze-up	Number of days with no data after landfast ice break-up
2002/03	36	0
2003/04	11	39
2004/05	1	7
2005/06	7	8
2006/07	8	3
2007/08	2	1
2008/09	0	0
2009/10	23	2
2010/11	1	1
2011/12	0	0
2012/13	2	2
2013/14	0	0
2014/15	1	2
2015/16	4	3
2016/17	0	1
2017/18	0	0
2018/19	0	0
2019/20	0	0
2020/21	0	0
2021/22	3	5
2022/23	3	1
2023/24	2	0
2024/25	1	0

602

603 The landfast ice break-up coincided with the time when pack ice was already absent (Fig. 9) and temperatures
 604 remained over the melting point for ca. 25 days. Interestingly both θ and thermodynamic ice thickness remained
 605 positive which may suggest that other processes play a key role in ice break-up. We suggest that these are waves,
 606 both swell/sea from the south-west and those locally generated by wind, that break the edges of the landfast ice
 607 and accelerate melting (Graham et al., 2019). The thermodynamic ice thickness at the time of the landfast ice
 608 break-up averaged 0.57 m. In situ ice ice thickness measurements, as well as local meteorological stations and
 609 moorings in the individual bays of Hornsund would help prove this hypothesis, enabling to account for local-scale
 610 differences in meteorological and oceanographic conditions, given the east-west gradient (Araźny et al., 2018)
 611 and topographic complexity.

612 **6 Conclusions**

613 The full archive of high-resolution SAR imagery (Envisat ASAR, RADARSAT-2 and Sentinel-1) fully covering
 614 Hornsund fjord between October 2002 and August 2025 was used to create an unprecedented set of near-daily
 615 binary ice/open water maps over the fjord area for 23 seasons. We observed a general trend of sea ice season



616 shortening by 2.3 days yr^{-1} , and a gradual decrease in average ice coverage during the sea ice season, particularly
617 in the main basin of Hornsund ($-1.6\% \text{ yr}^{-1}$), which we attributed to the general decrease in pack ice duration and
618 extend in the Arctic. The changes are smaller down to negligible for the landfast ice season and the inner bays of
619 the fjord, where landfast ice develops in situ. On the top of the longer-term trend, the results suggest a great
620 interannual variability in ice conditions, which are strongly related to the autumn (October-December) and/or
621 winter (January-March) air temperatures averaged from the observations at the Polish Polar Station. The length
622 of the sea ice season is shortened by 19.5 days for every 1°C increase in the mean autumn air temperature ($R^2 =$
623 0.61 , $p < 0.05$). Step-wise multiple linear regression showed that predicting ice conditions can be improved by
624 combining a range of meteorological and oceanographic parameters (air temperature, T , wind speed, WS , sea
625 surface temperature, SST and significant wave height, SWH) with SST having a similar but more subtle effect than
626 T , higher autumn WS characterising longer ice seasons and SWH showing weak but negative correlation with the
627 ice conditions.

628

629 In the period leading to the landfast ice freeze-up, T typically remained under the freezing point (-1.8°C) for over
630 90 days, decreasing gradually by $-0.1^\circ\text{C day}^{-1}$. At that time, the drift ice was present in the fjord, lowering the near
631 surface water temperature and protecting fjord waters from the incoming wave energy. In average, for 40 days
632 prior to the landfast ice formation the ice coverage exceeded 20%, rising to 26% on the day preceding the freeze-
633 up. The landfast ice break-up was characterised by a lack of drift ice and positive T for an average of 38 days with
634 a gradual increase of $0.1^\circ\text{C day}^{-1}$ over the 90-day period. Calculation of the sea ice thickness in thermodynamic
635 terms showed that the landfast ice is detectable on C-band SAR imagery when it is thicker than 0.33 m (range:
636 0.22-0.52 m) while the landfast ice break-up is related to other processes than only melting (such as breaking by
637 waves) since on the date identified as the landfast ice season end the thermodynamic thickness averaged 0.57 m.

638

639 This study provides open long-term (23 seasons) high spatial (50 m) and temporal (2 days) resolution dataset of
640 ice maps for any analyses including fjord hydrography, glacier/ocean interaction and ecology. It can help assess
641 wave impact on coastal change and safety for boat and snowmobile operations. Finally, because of its duration
642 and detail, it provides information on the changing climate of the Arctic and the impact of weather and oceanic
643 conditions on the state of ice.

644 **Data availability**

645 The binary ice/open water maps are available in the PANGAEA repository: those based on Envisat ASAR 2002-
646 2012 are at <https://doi.org/10.1594/PANGAEA.986427> (Papin et al., 2025a), those based on RADARSAT-2
647 2012-2016 are at <https://doi.pangaea.de/10.1594/PANGAEA.969031> (Swirad et al., 2024b), those based of
648 Sentinel-1A/B 2014-2023 are at <https://doi.org/10.1594/PANGAEA.963167> (Swirad et al., 2023a), and those
649 based on Sentinel-1A 2023-2025 are at <https://doi.org/10.1594/PANGAEA.987853> (Papin et al., 2025b).
650 Additionally, three erroneously classified images from Swirad et al. (2023a) are available at
651 <https://doi.org/10.5281/zenodo.17350297> (Swirad, 2025).



652 **Supplement**

653 Table S1 in the Supplement is the time series of the extent and coverage of ice in Hornsund and its parts. Table
654 S2 in the Supplement is a time series of meteorological and oceanographic conditions. Table S3 in the Supplement
655 is a summary of ice and climate parameters for individual seasons. Document S4 contains supplementary figures.

656 **Author contribution**

657 ZMS and AMJ conceptualised the study. EM pre-processed the SAR scenes. VP processed and analysed the data
658 with the help from ZS. VP and ZS wrote the original manuscript. All authors edited the manuscript and agreed on
659 its final version.

660 **Competing interests**

661 None of the authors has any competing interests.

662 **Acknowledgements**

663 We thank Meri Korhonen (IG PAS) for preparing meteorological data. Envisat ASAR and Sentinel-1 data are
664 freely available through the European Union's Earth observation Copernicus programme (<https://copernicus.eu>,
665 last access: 21 July 2025). RADARSAT-2 data was provided by NCS/KSAT under the Norwegian-Canadian
666 RADARSAT-2 agreement 2011–16. ERA5 data are freely available at the Climate Data Store website
667 (<https://cds.climate.copernicus.eu/>, last access: 17 November 2025).

668 **Financial support**

669 This study was funded by the European Space Agency (HIRLOMAP ESA Contract No. 4000146036/24/I-DT-
670 bgh). Vincent Papin's stay at IG PAS was partly funded by the European Union's Erasmus programme. Eirik
671 Malnes was partly funded by the European Space Agency (Svalbard Cryosphere Digital Twin - SvalbardDT, ESA
672 Contract No. 4000146232/24/I-KE).

673 **Bibliography**

674 Arażny, A., Przybylak, R., Wszyński, P., Wawrzyniak, T., Nawrot, A., and Budzik, T.: Spatial variations in air
675 temperature and humidity over Hornsund fjord (Spitsbergen) from 1 July 2014 to 30 June 2015, *Geografiska*
676 *Annaler Series a Physical Geography*, 100, 27–43, <https://doi.org/10.1080/04353676.2017.1368832>, 2017.
677 Barzycka, B., Grabiec, M., Błaszczuk, M., Ignatiuk, D., Laska, M., Hagen, J. O., Jania, J.: Changes of glacier
678 facies on Hornsund glaciers (Svalbard) during the decade 2007–2017, *Remote Sensing of Environment*, 251,
679 112060, <https://doi.org/10.1016/j.rse.2020.112060>, 2020.
680 Błaszczuk, M., Jania, J. A., and Kolondra, L.: Fluctuations of tidewater glaciers in Hornsund fjord (southern
681 Svalbard) since the beginning of the 20th century, *Polish Polar Research*, 34(4), 327–352,
682 <https://journals.pan.pl/dlibra/publication/114504/edition/99557/content> (last access: 24 March 2026), 2013.



- 683 Błaszczuk, M., Ignatiuk, D., Uszczyk, A., Cielecka-Nowak, K., Grabiec, M., Jania, J. A., Moskalik, M., and
684 Walczowski, W.: Freshwater input to the Arctic fjord Hornsund (Svalbard), *Polar Research*, 38,
685 <https://doi.org/10.33265/polar.v38.3506>, 2019.
- 686 Błaszczuk, M., Moskalik, M., Grabiec, M., Jania, J., Walczowski, W., Wawrzyniak, T., Strzelewicz, A., Malnes,
687 E., Lauknes, T. R., and Pfeffer, W. T.: The response of tidewater glacier Termini positions in Hornsund (Svalbard)
688 to climate forcing, 1992–2020, *Journal of Geophysical Research Earth Surface*, 128,
689 <https://doi.org/10.1029/2022jf006911>, 2023.
- 690 van den Broek, D., Urbancic, G.H., Rantanen, M., and Vihma, T.: Svalbard's record-breaking arctic summer 2024:
691 Anomalies beyond climatological warming trends, *Geophysical Research Letters*, 52, e2025GL115015,
692 <https://doi.org/10.1029/2025GL115015>, 2025.
- 693 Casas-Prat, M. and Wang, X. L.: Projections of extreme ocean waves in the Arctic and potential implications for
694 coastal inundation and erosion, *J. Geophys. Res. Oceans*, 125, e2019JC015745,
695 <https://doi.org/10.1029/2019JC015745>, 2020.
- 696 Cottier, F. R., Nilsen, F., Skogseth, R., Tverberg, V., Skarøhamar, J., and Svendsen, H.: Arctic fjords: a review of
697 the oceanographic environment and dominant physical processes, *Geological Society London Special
698 Publications*, 344, 35–50, <https://doi.org/10.1144/sp344.4>, 2010.
- 699 Cristea, A., Van Houtte, J., and Doulgeris, A. P.: Integrating incidence angle dependencies into the Clustering-
700 Based Segmentation of SAR images, *IEEE Journal of Selected Topics in Applied Earth Observations and Remote
701 Sensing*, 13, 2925–2939, <https://doi.org/10.1109/jstars.2020.2993067>, 2020.
- 702 Dahlke, S., Hughes, N., Wagner, P., Gerland, S., Wawrzyniak, T., Ivanov, B., and Maturilli, M.: The observed
703 recent surface air temperature development across Svalbard and concurring footprints in local sea ice cover, *Int.
704 J. Climatol.*, 40, 5246–5265, <https://doi.org/10.1002/joc.6517>, 2020.
- 705 Dobiński, W. and Kasprzak, M.: Permafrost base degradation: characteristics and unknown thread with specific
706 example from Hornsund, Svalbard, *Frontiers in Earth Science*, 10, <https://doi.org/10.3389/feart.2022.802157>,
707 2022.
- 708 Dong, Y., Xiao, P., Zhang, X. Ge, D., Yu, J., Chen, Y., Wu, Q., Ma, Y., Liu, R., Luan, W., Liu, H., and Bai, J.:
709 Increased vulnerability of Arctic potential ice roads under climate change, *Commun Earth Environ*, 6, 37,
710 <https://doi.org/10.1038/s43247-025-02011-y>, 2025.
- 711 Frank, L., Jonassen, M. O., Skogseth, R., and Vihma, T.: Atmospheric climatologies over Isfjorden, Svalbard,
712 *Journal of Geophysical Research Atmospheres*, 128, <https://doi.org/10.1029/2022jd038011>, 2023.
- 713 Fraser N. J., Skogseth R., Nilsen F., and Inall M. E.: Circulation and exchange in a broad Arctic fjord using glider-
714 based observations, *Polar Research*, 37, 1485417, <https://doi.org/10.1080/17518369.2018.1485417>, 2018.
- 715 Graham, R. M., Itkin, P., Meyer, A., Sundfjord, A., Spreen, G., Smedsrud, L. H., Liston, G. E., Cheng, B., Cohen,
716 L., Divine, D., Fer, I., Fransson, A., Gerland, S., Haapala, J., Hudson, S. R., Johansson, A. M., King, J.,
717 Merkouriadi, I., Peterson, A. K., Provost, C., Randelhoff, A., Rinke, A., Rösel, A., Sennéchaël, N., Walden, V.
718 P., Duarte, P., Assmy, P., Steen, H. and Granskog, M. A.: Winter storms accelerate the demise of sea ice in the
719 Atlantic sector of the Arctic Ocean, *Scientific Reports*, 9, 9222, <https://doi.org/10.1038/s41598-019-45574-5>,
720 2019.



- 721 Herman, A., Swirad, Z. M., and Moskalik, M.: Increased exposure of the shores of Hornsund (Svalbard) to wave
722 action due to a rapid shift in sea ice conditions, *Elementa Science of the Anthropocene*, 13,
723 <https://doi.org/10.1525/elementa.2024.00067>, 2025.
- 724 Herman, A., Wojtysiak, K., and Moskalik, M.: Wind wave variability in Hornsund fjord, west Spitsbergen, *Estuar.
725 Coast. Shelf S.*, 217, 96–109, <https://doi.org/10.1016/j.ecss.2018.11.001>, 2019.
- 726 Hersbach, H., Bell, B., Berrisford, P., Biavati, G., Horányi, A., Muñoz Sabater, J., Nicolas, J., Peubey, C., Radu,
727 R., Rozum, I., Schepers, D., Simmons, A., Soci, C., Dee, D., and Thépaut, J.-N.: ERA5 hourly data on single
728 levels from 1940 to present, Copernicus Climate Change Service Climate Data Store (CDS),
729 <https://doi.org/10.24381/cds.adbb2d47>, 2023 (last access: 8 October 2025).
- 730 IPCC: Climate Change 2023: Synthesis Report. Contribution of Working Groups I, II and III to the Sixth
731 Assessment Report of the Intergovernmental Panel on Climate Change [Core Writing Team, H. Lee and J. Romero
732 (eds.)]. IPCC, Geneva, Switzerland, 184 pp., doi: 10.59327/IPCC/AR6-9789291691647, 2023.
- 733 Itkin, P., Losch, M., and Gerdes, R.: Landfast ice affects the stability of the Arctic halocline: Evidence from a
734 numerical model, *Journal of Geophysical Research Oceans*, 120, 2622–2635,
735 <https://doi.org/10.1002/2014jc010353>, 2015.
- 736 Jakacki, J., Przyborska, A., Kosecki, S., Sundfjord, A., and Albrechtsen, J.: Modelling of the Svalbard fjord
737 Hornsund, *Oceanologia*, 59, 473–495, <https://doi.org/10.1016/j.oceano.2017.04.004>, 2017.
- 738 Jansen, E., Christensen, J. H., Dokken, T., Nisancioglu, K. H., Vinther, B. M., Capron, E., Guo, C., Jensen, M. F.,
739 Langen, P. L., Pedersen, R. A., Yang, S., Bentsen, M., Kjær, H. A., Sadatzki, H., Sessford, E., and Stendel, M.:
740 Past perspectives on the present era of abrupt Arctic climate change, *Nature Climate Change*, 10, 714–721,
741 <https://doi.org/10.1038/s41558-020-0860-7>, 2020.
- 742 Johansson, A. M., Malnes, E., Gerland, S., Cristea, A., Doulgeris, A. P., Divine, D. V., Pavlova, O., and Lauknes,
743 T. R.: Consistent ice and open water classification combining historical synthetic aperture radar satellite images
744 from ERS-1/2, Envisat ASAR, RADARSAT-2 and Sentinel-1A/B, *Annals of Glaciology*, 61, 40–50,
745 <https://doi.org/10.1017/aog.2019.52>, 2020.
- 746 Korhonen, M., Moskalik, M., Głowacki, O., and Jain, V.: Oceanographic monitoring in Hornsund fjord, Svalbard,
747 *Earth System Science Data*, 16, 4511–4527, <https://doi.org/10.5194/essd-16-4511-2024>, 2024.
- 748 Kowalik, Z., Marchenko, A., Brazhnikov, D., and Marchenko, N.: Tidal currents in the western Svalbard Fjords,
749 *Oceanologia*, 57, 318–327, <https://doi.org/10.1016/j.oceano.2015.06.003>, 2015.
- 750 Kwok, R.: Contrasts in sea ice deformation and production in the Arctic seasonal and perennial ice zones, *J.
751 Geophys. Res.*, 111, C11S22, <https://doi.org/10.1029/2005JC003246>, 2006.
- 752 Lebedev, V.: Rost l'da v arkticheskikh rekakh i moriakh v zavisimosti ot otritsatel'nykh temperatur vozdukha,
753 *Problemy Arktiki*, 5(6), 9–25, 1938.
- 754 Li, T., Hofer, S., Moholdt, G., Igneczi, A., Heidler, K., Zhu, X. X., and Bamber, J.: Pervasive glacier retreats
755 across Svalbard from 1985 to 2023, *Nat Commun* 16, 705, <https://doi.org/10.1038/s41467-025-55948-1>, 2025.
- 756 Mioduszewski, J., Vavrus, S., and Wang, M.: Diminishing Arctic Sea ice promotes stronger surface winds, *Journal
757 of Climate*, 31, 8101–8119, <https://doi.org/10.1175/jcli-d-18-0109.1>, 2018.
- 758 Muckenhuber, S., Nilsen, F., Korosov, A., and Sandven, S.: Sea ice cover in Isfjorden and Hornsund, Svalbard
759 (2000–2014) from remote sensing data, *The Cryosphere*, 10, 149–158, <https://doi.org/10.5194/tc-10-149-2016>,
760 2016.



- 761 NOAA: National Centers for Environmental Information, Climate at a Glance: Global Time Series,
762 <https://www.ncdc.noaa.gov/cag/>, last access: 15 June 2025.
- 763 Onarheim, I. H., Smedsrud, L. H., Ingvaldsen, R. B., and Nilsen, F.: Loss of sea ice during winter north of
764 Svalbard, *Tellus*, 66A, 23933, <https://doi.org/10.3402/tellusa.v66.23933>, 2014.
- 765 Papin, V., Swirad, Z. M., Johansson, A. M., and Malnes, E.: Ice distribution in Hornsund fjord, Svalbard from
766 Envisat ASAR (2002–2012), PANGAEA [data set], <https://doi.org/10.1594/pangaea.986427>, 2025a.
- 767 Papin, V., Swirad, Z. M., Johansson, A. M., and Malnes, E.: Ice distribution in Hornsund fjord, Svalbard from
768 Sentinel-1A (2023–2025), PANGAEA [data set], <https://doi.org/10.1594/PANGAEA.987853>, 2025b.
- 769 Park, J.-W., Korosov, A. A., Babiker, M., Won, J.-S., Hansen, M. W., and Kim, H.-C.: Classification of sea ice
770 types in Sentinel-1 synthetic aperture radar images, *The Cryosphere*, 14, 2629–2645, [https://doi.org/10.5194/tc-](https://doi.org/10.5194/tc-14-2629-2020)
771 14-2629-2020, 2020.
- 772 Pizzolato, L., Howell, S. E. L., Dawson, J., Laliberté, F., and Copland, L.: The influence of declining sea ice on
773 shipping activity in the Canadian Arctic, *Geophysical Research Letters*, 43,
774 <https://doi.org/10.1002/2016gl071489>, 2016.
- 775 Promińska, A., Falck, E., and Walczowski, W.: Interannual variability in hydrography and water mass distribution
776 in Hornsund, an Arctic fjord in Svalbard, *Polar Research*, 37, 1495546,
777 <https://doi.org/10.1080/17518369.2018.1495546>, 2018.
- 778 Rinke, A., Maturilli, M., Graham, R. M., Matthes, H., Handorf, D., Cohen, L., Hudson, S. R., and Moore, J. C.:
779 Extreme cyclone events in the Arctic: Wintertime variability and trends, *Environmental Research Letters*, 12,
780 094006, <https://doi.org/10.1088/1748-9326/aa7def>, 2017.
- 781 Shulman, I., Jarosz, E., Cayula, S., and Metzger, E. J.: Dynamics of the Polar Front in the southwestern area of
782 Svalbard, Norway, *Ocean Dynamics*, 74(8), 637–653, <https://doi.org/10.1007/s10236-024-01624-9>, 2024.
- 783 Smith, L. C. and Stephenson, S. R.: New Trans-Arctic shipping routes navigable by midcentury, *Proceedings of*
784 *the National Academy of Sciences*, 110, E1191-5, <https://doi.org/10.1073/pnas.1214212110>, 2013.
- 785 de Steur, L., Sumata, H., Divine, D. V., Granskog, M. A., and Pavlova O.: Upper ocean warming and sea ice
786 reduction in the East Greenland Current from 2003 to 2019, *Commun. Earth Environ.*, 4, 261,
787 <https://doi.org/10.1038/s43247-023-00913-3>, 2023.
- 788 Stocker, A. N., Renner, A. H. H., and Knol-Kauffman, M.: Sea ice variability and maritime activity around
789 Svalbard in the period 2012–2019, *Scientific Reports*, 10, 17043, <https://doi.org/10.1038/s41598-020-74064-2>,
790 2020.
- 791 Strzelewicz, A., Przyborska, A., and Walczowski, W.: Increased presence of Atlantic Water on the shelf south-
792 west of Spitsbergen with implications for the Arctic fjord Hornsund, *Progress in Oceanography*, 200, 102714,
793 <https://doi.org/10.1016/j.pocean.2021.102714>, 2021.
- 794 Su, H., and Y. Wang: Using MODIS data to estimate sea ice thickness in the Bohai Sea (China) in the 2009–2010
795 winter, *J. Geophys. Res.*, 117, C10018, <https://doi.org/10.1029/2012JC008251>, 2012.
- 796 Svendsen, H., Beszczynska-Møller, A., Hagen, J. O., Lefauconnier, B., Tverberg, V., Gerland, S., Ørbæk, J. B.,
797 Bischof, K., Papucci, C., Zajaczkowski, M., Azzolini, R., Bruland, O., and Wiencke, C.: The physical environment
798 of Kongsfjorden–Krossfjorden, an Arctic fjord system in Svalbard, *Polar Research*, 21, 133–166,
799 <https://doi.org/10.3402/polar.v21i1.6479>, 2002.



- 800 Swerpel, S.: The Hornsund Fjord: water masses, *Polish Polar Research*, 6(4),
801 <https://journals.pan.pl/Content/111444> (last access: 24 March 2026), 1985.
- 802 Swirad, Z. M.: Correction to the “Ice distribution in Hornsund fjord, Svalbard from Sentinel-1A/B (2014–2023)”
803 dataset, Zenodo [data set], <https://doi.org/10.5281/zenodo.17350297>, 2025.
- 804 Swirad, Z. M., Johansson, A. M., and Malnes, E.: Ice distribution in Hornsund fjord, Svalbard from Sentinel-1A/B
805 (2014–2023), PANGAEA [data set], <https://doi.org/10.1594/PANGAEA.963167>, 2023a.
- 806 Swirad, Z. M., Moskalik, M., and Herman, A.: Wind wave and water level dataset for Hornsund, Svalbard (2013–
807 2021), *Earth System Science Data*, 15(6), 2623–2633, <https://doi.org/10.5194/essd-15-2623-2023>, 2023b.
- 808 Swirad, Z. M., Johansson, A. M., and Malnes, E.: Extent, duration and timing of the sea ice cover in Hornsund,
809 Svalbard, from 2014–2023, *The Cryosphere*, 18(2), 895–910, <https://doi.org/10.5194/tc-18-895-2024>, 2024a.
- 810 Swirad, Z. M., Johansson, A. M., and Malnes, E.: Ice distribution in Hornsund fjord, Svalbard from RADARSAT-
811 2 (2012–2016), PANGAEA [data set], <https://doi.org/10.1594/PANGAEA.969031>, 2024b.
- 812 Swirad Z. M., Herman A., and Moskalik M.: Sub-monthly to inter-annual Arctic gravel beach change and
813 controlling factors, EGU General Assembly 2026, Vienna, Austria, 3–8 May 2026, EGU26-2311,
814 <https://doi.org/10.5194/egusphere-egu26-2311>, 2026a.
- 815 Swirad, Z. M., Johansson, A. M., and Malnes, E.: Distribution of landfast, drift and glacier ice in Hornsund,
816 Svalbard, *The Cryosphere*, 20, 113–134, <https://doi.org/10.5194/tc-20-113-2026>, 2026b.
- 817 Wakabayashi, H., Matsuoka, T., Nakamura, K., and Nishio, F.: Polarimetric Characteristics of sea ice in the sea
818 of Okhotsk observed by airborne L-band SAR, *IEEE Transactions on Geoscience and Remote Sensing*, 42(11),
819 2412–2425, <https://doi.org/10.1109/TGRS.2004.836259>, 2024.
- 820 Wawrzyniak, T. and Osuch, M.: A 40-year High Arctic climatological dataset of the Polish Polar Station Hornsund
821 (SW Spitsbergen, Svalbard), *Earth System Science Data*, 12, 805–815, <https://doi.org/10.5194/essd-12-805-2020>,
822 2020.
- 823 Wojtysiak, K., Herman, A., and Moskalik, M.: Wind wave climate of west Spitsbergen: seasonal variability and
824 extreme events, *Oceanologia*, 60, 331–343, <https://doi.org/10.1016/j.oceano.2018.01.002>, 2018.
- 825 Zagórski, P., Rodzik, J., Moskalik, M., Strzelecki, M. C., Lim, M., Błaszczyk, M., Promińska, A., Kruszewski,
826 G., Styszyńska, A., and Malczewski, A.: Multidecadal (1960–2011) shoreline changes in Isbjørnhamna
827 (Hornsund, Svalbard), *Polish Polar Research*, 36(4), 369–390, <https://journals.pan.pl/Content/99617> (last access:
828 24 March 2026), 2015.
- 829 Zakhvatkina, N., Korosov, A., Muckenhuber, S., Sandven, S., and Babiker, M.: Operational algorithm for ice–
830 water classification on dual-polarized RADARSAT-2 images, *The Cryosphere*, 11, 33–46,
831 <https://doi.org/10.5194/tc-11-33-2017>, 2017.